



Patchy Nightside Clouds on Ultra-hot Jupiters: General Circulation Model Simulations with Radiatively Active Cloud Tracers

Thaddeus D. Komacek^{1,5} , Xianyu Tan^{2,5} , Peter Gao^{3,6} , and Elspeth K. H. Lee^{4,6} ¹ Department of Astronomy, University of Maryland, College Park, MD 20742, USA; tkomacek@umd.edu² Atmospheric, Oceanic and Planetary Physics, Department of Physics, University of Oxford, OX1 3PU, UK³ Earth and Planets Laboratory, Carnegie Institution for Science, 5241 Broad Branch Road, NW, Washington, DC 20015, USA⁴ Center for Space and Habitability, University of Bern, Gesellschaftsstrasse 6, CH-3012 Bern, Switzerland

Received 2022 February 21; revised 2022 May 14; accepted 2022 June 7; published 2022 July 27

Abstract

The atmospheres of ultra-hot Jupiters have been characterized in detail through recent phase curve and low- and high-resolution emission and transmission spectroscopic observations. Previous numerical studies have analyzed the effect of the localized recombination of hydrogen on the atmospheric dynamics and heat transport of ultra-hot Jupiters, finding that hydrogen dissociation and recombination lead to a reduction in the day-to-night contrasts of ultra-hot Jupiters relative to previous expectations. In this work, we add to previous efforts by also considering the localized condensation of clouds in the atmospheres of ultra-hot Jupiters, their resulting transport by the atmospheric circulation, and the radiative feedback of clouds on the atmospheric dynamics. To do so, we include radiatively active cloud tracers into the existing MITgcm framework for simulating the atmospheric dynamics of ultra-hot Jupiters. We take cloud condensate properties appropriate for the high-temperature condensate corundum from CARMA cloud microphysics models. We conduct a suite of general circulation model (GCM) simulations with varying cloud microphysical and radiative properties, and we find that partial cloud coverage is a ubiquitous outcome of our simulations. This patchy cloud distribution is inherently set by atmospheric dynamics in addition to equilibrium cloud condensation, and causes a cloud greenhouse effect that warms the atmosphere below the cloud deck. Nightside clouds are further sequestered at depth due to a dynamically induced high-altitude thermal inversion. We post-process our GCMs with the Monte Carlo radiative transfer code gCMCRT and find that the patchy clouds on ultra-hot Jupiters do not significantly impact transmission spectra but can affect their phase-dependent emission spectra.

Unified Astronomy Thesaurus concepts: [Exoplanet atmospheres \(487\)](#); [Hot Jupiters \(753\)](#); [Planetary atmospheres \(1244\)](#); [Atmospheric clouds \(2180\)](#)

1. Introduction

Ultra-hot Jupiters are a novel class of substellar objects with atmospheres that lie in a regime between the cooler hot Jupiters and those of late-type stars. These gaseous exoplanets orbit extremely close to their host star, with zero albedo full-redistribution equilibrium temperatures in excess of 2200 K. The enormous incident stellar flux that ultra-hot Jupiters receive along with their likely tidally synchronized rotational state cause a large day-to-night temperature contrast akin to cooler hot Jupiters, which in turn is predicted to generate planetary-scale waves that drive an eastward equatorial jet (Showman & Polvani 2011; see recent reviews of the atmospheric circulation of extrasolar gas giant planets by Showman et al. (2020), Zhang (2020), Fortney et al. (2021)). As a result, the present theoretical understanding of ultra-hot Jupiters relies upon extensions of numerical general circulation models (GCMs) developed to understand their cooler cousins (e.g., Parmentier et al. 2018; Tan & Komacek 2019; Beltz et al. 2021; May et al. 2021). However, a variety of processes that are either inactive or weak in the atmospheres of standard hot

Jupiters are expected to affect the atmospheric structure and dynamics of ultra-hot Jupiters, necessitating a coupled framework to develop further understanding.

The most prominent difference between the atmospheres of hot and ultra-hot Jupiters is expected to be the thermal dissociation of molecular species (Kitzmann et al. 2018; Lothringer et al. 2018; Parmentier et al. 2018), for which there is observational evidence in a wide range of low-resolution transmission spectra, emission spectra, and phase curves to date (Stevenson et al. 2014; Haynes et al. 2015; Beatty et al. 2017; Evans et al. 2017; Sheppard et al. 2017; Arcangeli et al. 2018; Kreidberg et al. 2018; Mansfield et al. 2018; Baxter et al. 2020; Gandhi et al. 2020; Mansfield et al. 2020; Mikal-Evans et al. 2020; Wilson et al. 2020; Wong et al. 2020; Fu et al. 2021; Mansfield et al. 2021; Changeat 2022; Mikal-Evans et al. 2022). Thermal dissociation also affects the primary atmospheric constituent of ultra-hot Jupiters, molecular hydrogen, causing dissociation of molecular hydrogen to atomic form on the hot dayside, and recombination of molecular hydrogen on the cooler limbs and nightside (Bell & Cowan 2018; Komacek & Tan 2018; Tan & Komacek 2019; Gandhi & Jermyn 2020; Roth et al. 2021). The thermodynamic impact of hydrogen dissociation and recombination shapes the atmospheric structure and dynamics of ultra-hot Jupiters, reducing day–night temperature contrasts and affecting the planetary-scale standing wave pattern of ultra-hot Jupiters, leading to a reduction in the speed of the equatorial jet (Bell & Cowan 2018; Tan & Komacek 2019).

⁵ T.D.K. and X.T. contributed equally to this work.⁶ P.G. and E.K.H.L. contributed equally to this work.

Original content from this work may be used under the terms of the [Creative Commons Attribution 4.0 licence](#). Any further distribution of this work must maintain attribution to the author(s) and the title of the work, journal citation and DOI.

A variety of other processes along with molecular dissociation conspire to set the atmospheric structure and dynamics of ultra-hot Jupiters. This includes absorption of incident stellar radiation by atomic metals in the planetary atmosphere that can lead to “inverted” temperature–pressure profiles, which increase in temperature with decreasing pressure (Fortney et al. 2008; Lothringer et al. 2018; Kitzmann et al. 2018; Gandhi & Madhusudhan 2019; Malik et al. 2019) and can be especially strong for ultra-hot Jupiters that orbit early-type stars (Lothringer & Barman 2019; Fu et al. 2022). Recent high-spectral-resolution observations of ultra-hot Jupiters have found a wealth of metallic species along with evidence for thermal inversions (Nugroho et al. 2017; Hoeijmakers et al. 2018; Jensen et al. 2018; Seidel et al. 2019; Cabot et al. 2020; Ehrenreich et al. 2020; Hoeijmakers et al. 2020; Nugroho et al. 2020; Pino et al. 2020; Yan et al. 2020; Kasper et al. 2021; Kesseli & Snellen 2021; Prinoth et al. 2022; Tabernero et al. 2021; Yan et al. 2022). The hot daysides of ultra-hot Jupiters should be sufficiently ionized that magnetohydrodynamic mechanisms can affect their atmospheric circulation (Perna et al. 2010; Menou 2012; Batygin et al. 2013; Rauscher & Menou 2013; Rogers & Showman 2014; Rogers & Komacek 2014; Hindle et al. 2019; Beltz et al. 2022), potentially causing large-amplitude time-variability due to induced atmospheric magnetic fields (Rogers 2017; Rogers & Mcelwaine 2017; Hindle et al. 2021a, 2021b). Additionally, many ultra-hot Jupiters are highly inflated, indicating a significant internal heat flux (Thorngren & Fortney 2018; Thorngren et al. 2019; Sarkis et al. 2021), which can affect their deep atmospheric circulation and mixing (Tremblin et al. 2017; Sainsbury-Martinez 2019; Carone et al. 2020; Baeyens et al. 2021).

Along with molecular dissociation, atomic metal absorption, thermal ionization and magnetohydrodynamic effects, and internal heating, one other process likely acts to shape the emergent properties of ultra-hot Jupiters: aerosol coverage. Unlike the other processes at work in ultra-hot Jupiter atmospheres, aerosols and their radiative feedback on the circulation likely have a more minor effect on the atmospheric dynamics of ultra-hot Jupiters than for hot Jupiters due to the high temperatures preventing condensation of many mineral species (for a comprehensive recent review of exoplanet aerosols, see Gao et al. 2021). Given the high temperatures on the daysides of both hot and ultra-hot Jupiters and large horizontal temperature contrasts, it is expected that their aerosol coverage is nonuniform, with enhanced condensate cloud coverage on the cooler western limb and nightside and with haze distributions dependent on particle size (Helling et al. 2016; Parmentier et al. 2016; Kempton et al. 2017; Wakeford et al. 2017; Mendonca et al. 2018; Powell et al. 2018, 2019; Gao et al. 2020; Adams et al. 2022; Helling et al. 2021; Parmentier et al. 2021; Roman et al. 2021; Steinrueck et al. 2021; Robbins-Blanch et al. 2022). There is observational evidence of such nonuniform aerosol distributions from the reflected light signature in Kepler phase curves (Demory et al. 2013; Esteves et al. 2015; Hu et al. 2015; Schwartz & Cowan 2015; Parmentier et al. 2016), and both low- and high-resolution transmission spectra have been suggestive of nonuniform aerosol coverage that changes with local atmospheric temperature (Line & Parmentier 2016; Sing et al. 2016; Ehrenreich et al. 2020).

Though hot Jupiters have nonuniform dayside aerosol distributions, they are expected to have a thick nightside

condensate cloud deck that acts to reduce their outgoing long-wave radiation, producing the weak observed trend in nightside infrared brightness temperature with increasing equilibrium temperature (Beatty et al. 2019; Keating et al. 2019; Bell et al. 2021). This “flat nightside temperature” trend may be analogous to the “fixed anvil temperature” hypothesis proposed to explain the independence of outgoing long-wave radiation on the global-mean temperature of our warming Earth (Hartmann & Larson 2002; Kuang & Hartmann 2007; Zelinka & Hartmann 2010), as both rely on an increase in the cloud-top altitude with increasing planetary-mean temperature to mute the changes in outgoing long-wave radiation (Gao & Powell 2021). The observed flat nightside trend breaks and abruptly steepens in the ultra-hot Jupiter regime, potentially due to the dissipation of the uniform nightside cloud deck (Parmentier et al. 2021; Roman et al. 2021) or changes in the heat transport properties of ultra-hot Jupiters, which may be analogous to the more complex interplay between clouds, circulation, and climate found in modern cloud resolving models of Earth (Seeley et al. 2019; Wing et al. 2020) than expected in the framework of a fixed anvil cloud temperature.

The observational evidence for nonuniform aerosol distributions in hot and ultra-hot Jupiter atmospheres necessitates three-dimensional models of their coupled atmospheric circulation and aerosol distribution. A range of models have been developed that incorporate the radiative feedback of aerosols on the atmospheric circulation of hot Jupiters (Lee et al. 2016; Lines et al. 2018, 2019; Roman & Rauscher 2019; Parmentier et al. 2021; Roman et al. 2021; Christie et al. 2021). Models that include cloud-radiative feedback are especially critical for understanding the behavior of patchy clouds on atmospheric circulation. This is because patchy clouds lead to spatially inhomogeneous cloud-radiative forcing, with a cloud greenhouse effect caused by the weak outgoing long-wave radiation at cloud tops and enhanced cooling in cloud-free regions.

A substellar regime in which patchy cloud formation, cloud-radiative feedback, and vertical mixing of both clouds and chemical species have been studied in detail is that of brown dwarfs and directly imaged giant planets (Ackerman & Marley 2001; Freytag et al. 2010; Morley et al. 2012; Showman & Kaspi 2013; Morley et al. 2014; Bordwell et al. 2018; Tan & Showman 2019, 2021a, 2021b; Tremblin et al. 2021). Notably, Tan & Showman (2021a, 2021b) studied the effect of cloud-radiative feedback on the atmospheric dynamics of brown dwarfs, finding that cloud-radiative feedback can be a key driver of the atmospheric dynamics and inhomogeneous cloud structures as expected from analytic theory of cloud-radiative instability (Gierasch et al. 1973). Models of the global circulation of brown dwarfs (Showman et al. 2019; Tan & Showman 2021b; Tan 2022) predict significant variability due to a combination of gravity waves generated by interaction with the convective interior and cloud-radiative feedback. Such variability has been observed in a range of brown dwarfs to date (e.g., Gelino et al. 2002; Artigau et al. 2009; Radigan et al. 2012; Biller et al. 2013; Crossfield et al. 2014; Faherty et al. 2014; Karalidi et al. 2016; Lew et al. 2016; Apai et al. 2017; Allers et al. 2020; Vos et al. 2022), providing evidence that cloud patchiness and large-scale wave motions induce the observed variability. Additionally, the observational characterization of highly irradiated brown dwarfs orbiting white dwarfs (e.g., Casewell et al. 2018, 2020; Lew et al. 2022; Zhou et al. 2022) has recently motivated numerical models of their

atmospheric circulation (Lee et al. 2020; Tan & Showman 2020; Sainsbury-Martinez et al. 2021). Their atmospheric dynamics are expected to be unique given their placement in parameter space as hot and high-gravity objects with large internal heat fluxes, which motivates further understanding as a population analogous to ultra-hot Jupiters (Showman et al. 2020).

Nascent studies of the effect of patchy clouds on the observable properties of ultra-hot Jupiters have leveraged improved instrumental capabilities to probe planetary atmospheres with high temporal and spatial resolution and at short wavelengths. Recent near-ultraviolet (NUV) spectra of ultra-hot Jupiters have been studied to probe the temperature at which clouds condense at the terminator of hot Jupiters (Lothringer et al. 2020), with the hotter WASP-121b and WASP-178b showing evidence of a cloud-free limb (Sing et al. 2019; Lothringer et al. 2022) but spectra of the cooler HAT-P-41b (Lewis et al. 2020; Wakeford et al. 2020) signaling the presence of clouds. Contemporaneously, time-resolved high-spectral-resolution transit observations have found evidence for nonuniform absorption during the transits of WASP-76b (Ehrenreich et al. 2020; Kesseli & Snellen 2021; Seidel et al. 2021; Kesseli et al. 2022) and WASP-121b (Borsa et al. 2021). Due to the influence of atmospheric climate dynamics on the shape and wavelength of spectral lines (Kempton & Rauscher 2012; Showman et al. 2013; Kempton et al. 2014; Zhang et al. 2017; Seidel et al. 2020), high-spectral-resolution observations require three-dimensional models to fully extract the information embedded in the spectrum about the planetary atmosphere (Flowers et al. 2019; Beltz et al. 2021). Three-dimensional climate dynamics and radiative transfer modeling has recently been applied to study the observed time-resolved high-resolution transmission spectrum of WASP-76b (Wardnier et al. 2021; Savel et al. 2022), and demonstrate the influence of the atmospheric temperature, winds, and aerosol coverage on the resulting observable spectrum.

Recent Transiting Exoplanet Survey Satellite (TESS) discoveries and Spitzer characterization have enabled the study of hot and ultra-hot Jupiters as a population (see Figure 17 of Wong et al. (2021)). These discoveries include TOI-1431b, which is a young (≈ 0.3 Ga) ultra-hot Jupiter with an equilibrium temperature of ≈ 2370 K that was discovered and characterized by Addison et al. (2021) and Stangret et al. (2021). TOI-1431b lies in the regime just hotter than the transition point from hot to ultra-hot Jupiters, and similar to HAT-P-7b (Bell et al. 2021) it has a surprisingly small day-to-night temperature contrast due to an observed high nightside brightness temperature in the TESS bandpass. As a result, TOI-1431b is an ideal case study of the impact of the confluence of molecular dissociation, cloud coverage, and youth on the atmospheric circulation of ultra-hot Jupiters. In this work, we leverage TOI-1431b as a test case to study the combination of the thermodynamic effect of molecular dissociation and recombination and cloud-radiative feedback on the atmospheric circulation, cloud transport, and observable properties of ultra-hot Jupiters. To do so, we add radiatively active condensate cloud tracers to the existing ultra-hot Jupiter MITgcm with thermodynamically active atomic hydrogen tracers (Tan & Komacek 2019). We utilize CARMA cloud microphysics simulations (Gao et al. 2020; Gao & Powell 2021) to determine microphysical properties relevant for both the mixing of cloud tracers and their radiative feedback on the atmosphere. We then

apply the gCMCRT Monte Carlo radiative transfer code (Lee et al. 2022) to post-process our GCM simulations and make predictions for the impact of high-temperature cloud condensates on the observable properties of ultra-hot Jupiters.

The outline of this work is as follows. Section 2 describes the setup of the GCM simulations conducted in this work, including evolutionary calculations to determine the internal heat flux, implementation of radiatively active cloud tracers, and the GCM parameter sweep that we carry out. We describe the resulting atmospheric dynamics and cloud coverage from our GCMs in Section 3 along with the effects of clouds on emergent spectra and phase curves of ultra-hot Jupiters. We discuss the potential implications of our model results for the understanding of the effect of clouds on observations of ultra-hot Jupiters in Section 4, and describe present limitations of our model along with possible improvements to our current modeling framework. Lastly, we denote conclusions in Section 5.

2. Model Setup

2.1. MESA Evolutionary Models

In order to determine the temperature structure near the bottom of our GCM domain, we conducted a suite of planetary evolution calculations with the MESA stellar and planetary evolution code (Paxton et al. 2011, 2013, 2015, 2018, 2019). These planetary evolution calculations have an setup similar to that in Komacek & Youdin (2017) and Komacek et al. (2020), and solve the stellar structure equations (Chandrasekhar 1939; Kippenhahn et al. 2013), including mass conservation, hydrostatic equilibrium, energy conservation, and energy transport. The key modifications to the stellar structure equations in our model framework are the inclusion of an external irradiation by adding an energy generation rate in a specified outer column mass of the atmosphere, and the addition of an extra heating term in the interior spread as a Gaussian with a standard deviation of one-half a pressure scale height centered at a given pressure (see also Wu & Lithwick 2013; Millholland 2019; Mol Lous & Miguel 2020; Glanz et al. 2022). These models do not include a central heavy element core, and as a result prescribe upper limits on planetary radius (Bodenheimer et al. 2001; Guillot & Showman 2002; Thorngren et al. 2016) for a given planetary mass, irradiation, and amount of deposited heating in the interior.

As in Komacek et al. (2020), we include the time-varying irradiation due to stellar evolution in our planetary evolution calculations. We take the time-dependent stellar luminosity of TOI-1431 from Modules for Experiments in Stellar Astrophysics (MESA) Isochrones and Stellar Tracks (Choi et al. 2016; Dotter 2016) models with an initial mass of $1.895 M_{\odot}$, metallicity of $[\text{Fe}/\text{H}] = 0.43$, and a rotation rate of $v/v_{\text{crit}} = 0.4$. We apply irradiation in an outer mass column of 300 g cm^{-2} , taking the semimajor axis of TOI-1431b to be 0.0471 au . We assume full heat redistribution, allowing our planetary evolution calculations to represent the global-mean energy budget. The left-hand panel of Figure 1 displays the evolution of the effective temperature of TOI-1431b, showing the impacts of the early evolution of TOI-1431 on the irradiation received by TOI-1431b. Note that we show results from each MESA model to an age of 0.61 Gyr , consistent with the 1σ upper limit on the system age (Addison et al. 2021).

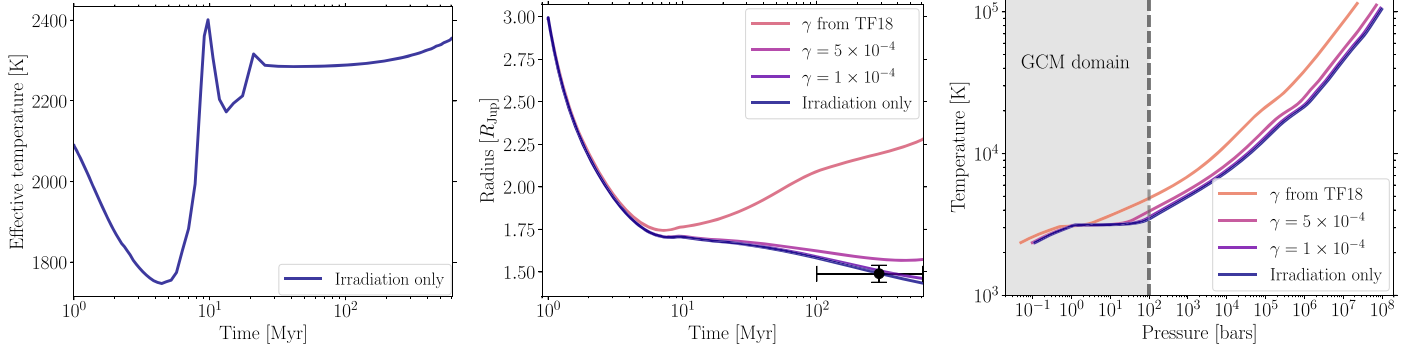


Figure 1. Evolution and final internal temperature structure for TOI-1431b models undergoing irradiation and varying levels of deposited heating. The left-hand panel shows the time evolution of the effective temperature, the central panel the radius evolution, and the right-hand panel the temperature–pressure profile for varying assumptions of the fraction of incident stellar flux converted to deposited heat, γ . The lightest colored line shows the case with a γ dependence on the incident stellar flux as derived from the full sample of hot Jupiters (Thorngren & Fortney 2018). The observed radius and age of TOI-1431b (Addison et al. 2021) is overplotted on the radius evolution track. Models with weak or no deposited heating are consistent with the present-day radius of TOI-1431b.

We include a fraction of the irradiation power, γ as deposited heating in the deep interior of the planet. As a result, the total amount of heat deposited in the interior of the planet, Γ , depends on γ and the incident stellar power as

$$\Gamma = \gamma L_{\text{irr}} = \pi \gamma R_p^2 F_*, \quad (1)$$

where L_{irr} is the incident stellar power, R_p is the planetary radius, and F_* is the incident stellar flux. Note that we include the positive feedback between planetary radius and deposited heat due to the increasing cross-sectional area of the planet (Batygin et al. 2011). We conduct a suite of models with varying γ from 0 to 5×10^{-4} , along with a simulation with time-varying γ following the dependence of internal heating on the incident stellar flux derived from the full suite of hot Jupiters (Equation (34) of Thorngren & Fortney (2018)). For all cases, we assume that the maximum of heat deposition occurs at the very center of the planet, in line with our motivation described above to set upper limits on the predicted planetary radius for a given heating rate in our model. We assume a planet mass of $3.12 M_{\text{Jup}}$ (Addison et al. 2021) for all cases, and we vary the initial planet radius from 2.5 – $4 R_{\text{Jup}}$ given the unknown initial entropy post-formation (Marleau & Cumming 2014; Berardo et al. 2017). We find that the assumed initial radius does not affect the present-day properties of TOI-1431b due to its short ($\lesssim 10$ Myr) Kelvin–Helmholtz contraction timescale (Ginzburg & Sari 2015; Mol Lous & Miguel 2020)—as a result, we only display results from the case with an intermediate initial radius of $3 R_{\text{Jup}}$.

Figure 1 shows the radius evolution and final temperature structures from evolutionary calculations of TOI-1431b with varied assumptions for the deposited heat in the interior. As in Addison et al. (2021), we find that TOI-1431b is underinflated for its age, with a present-day radius that can be fit either with only irradiation acting to slow cooling, a weak amount of incident stellar flux converted to heat in the deep interior, or if the planet did not form at its current location, but migrated inward (Mol Lous & Miguel 2020). The efficiency of conversion of incident stellar power to deposited heat (γ) expected from the suite of hot Jupiters overpredicts the present-day radius, either implying that the mechanism that inflates the majority of hot Jupiters is weaker than expected in TOI-1431b

or that it does not apply over the full evolution of TOI-1431b. TOI-1431b has a deep radiative envelope in models with weak or zero deposited internal heating, with radiative-convective boundaries between 104.4 and 43.5 bar with increasing γ from 0 to 5×10^{-4} . We further constrain the 100 bar temperature at the end of our evolutionary calculations to lie between 3459–3894 K with varying γ from 0 to 5×10^{-4} . Given the uncertainty in system age and heating rate, we take an intermediate value for the 100 bar temperature of 3750 K to prescribe the bottom boundary condition in our GCM simulations, as described below.

2.2. MITgcm Simulations

2.2.1. Double-gray GCM Framework with Radiatively Active Cloud Tracers

For the GCM simulations conducted in this work, we solve the three-dimensional primitive equations of meteorology with the MITgcm (Adcroft et al. 2004) including the thermodynamic impact of hydrogen dissociation and recombination (Tan & Komacek 2019; Mansfield et al. 2020; May et al. 2021). These include the equations of horizontal momentum, local hydrostatic equilibrium, mass conservation, energy conservation, and the ideal gas law as an equation of state, as follows:

$$\frac{dv}{dt} = -f\hat{k} \times v - \nabla_p \Phi + \mathcal{F}_{\text{drag}} + \mathcal{D}_S, \quad (2)$$

$$\frac{\partial \Phi}{\partial p} = -\frac{1}{\rho}, \quad (3)$$

$$\nabla_p \cdot v + \frac{\partial \omega}{\partial p} = 0, \quad (4)$$

$$\frac{d\theta'}{dt} = \frac{\theta'}{\bar{c}_p T} \left(g \frac{\partial F}{\partial p} + \frac{L_H \delta q_H}{\tau_{\text{relax}}} \right) + \mathcal{H}_{\text{drag}} + \mathcal{E}_S, \quad (5)$$

$$p = \rho \bar{R} T. \quad (6)$$

Symbols used in Equations (2)–(6) above include the pressure p , the horizontal velocity vector on isobars v , the vertical velocity in pressure coordinates $\omega = dp/dt$, the horizontal gradient on an isobar ∇_p , the total (material) derivative $d/dt = \partial/\partial t + v \cdot \nabla_p + \omega \partial/\partial p$, the Coriolis parameter $f = 2\Omega \sin \phi$, where Ω is planetary rotation rate and ϕ is latitude, the local vertical unit vector \hat{k} , the geopotential

$\Phi = gz$, where g is the gravity and z is the altitude, the mean gas density ρ , the mass-weighted specific gas constant and heat capacity \bar{R} and \bar{c}_p , the temperature T , the modified potential temperature $\theta' = T(p_0/p)^{\bar{R}/\bar{c}_p}$ with a reference pressure p_0 , the net radiative flux F , the recombination energy of hydrogen L_H , the mass mixing ratio of atomic hydrogen relative to the total air mass q_H , and the relaxation timescale of atomic hydrogen τ_{relax} . The change in atomic hydrogen mass mixing ratio due to H–H₂ conversion δq_H is detailed in Equation (15). Note that model parameter choices are shown in Table 1.

The $\mathcal{F}_{\text{drag}}$ term in Equation (2) corresponds to a frictional Rayleigh drag applied throughout the atmosphere as

$$\mathcal{F}_{\text{drag}} = -\frac{v}{\tau_{\text{drag}}}, \quad (7)$$

where τ_{drag} is a height-independent drag timescale. The kinetic energy dissipated via frictional drag is converted back into thermal energy as indicated by the $\mathcal{H}_{\text{drag}}$ term in Equation (5). The \mathcal{D}_S term in Equation (2) represents a high-order Shapiro filter that acts to damp the momentum of subgrid scale flow and prevent kinetic energy buildup at large wavenumbers, and the \mathcal{E}_S term in Equation (5) represents the conversion of kinetic to thermal energy by the Shapiro filter.

We couple the primitive equations of motion to tracer equations for the transport of condensable vapor and cloud condensate (Tan & Showman 2021a, 2021b):

$$\frac{dq_v}{dt} = (1 - s) \frac{\min(q_s - q_v, q_c)}{\tau_c} - s \frac{(q_v - q_s)}{\tau_c} - \frac{q_v - q_{\text{deep}}}{\tau_{\text{deep}}}, \quad (8)$$

$$\frac{dq_c}{dt} = s \frac{(q_v - q_s)}{\tau_c} - (1 - s) \frac{\min(q_s - q_v, q_c)}{\tau_c} - \frac{\partial(q_c \langle V_p \rangle)}{\partial p}. \quad (9)$$

Symbols used in Equations (8) and (9) include the mass mixing ratio of condensable vapor relative to the background hydrogen–helium air q_v , the mass mixing ratio of cloud condensate particles q_c , the mass mixing ratio of condensable vapor at saturation q_s , the supersaturation indicator s , which is set to one when vapor is supersaturated and zero if vapor is subsaturated, the cloud and condensable vapor tracer relaxation timescale τ_c , the deep vapor mass mixing ratio q_{deep} , the deep vapor replenishment timescale τ_{deep} , and the terminal settling velocity in pressure coordinates that is properly averaged over the particle size distribution $\langle V_p \rangle$. In this work, we take τ_c to be 15 s, slightly longer than the time step of the dynamical core and the same as the relaxation timescale τ_{relax} for the atomic hydrogen tracer. We do so because microphysical interconversion (evaporation and nucleation) timescales are generally much shorter than dynamical timescales in gas giant atmospheres (Helling & Casewell 2014; Gao & Benneke 2018; Powell et al. 2018). However, our model does not include condensational growth, which can occur on timescales that are comparable to or longer than the dynamical timescale in hot Jupiter atmospheres (Powell et al. 2018). Additionally, note that we do not include the thermodynamic impact of latent heat release from cloud condensation given its negligible magnitude in the ultra-hot Jupiter regime (Tan & Showman 2017).

Table 1
Planetary and Atmospheric Properties Assumed for The Suite of GCM Simulations Presented in This Work

Parameter	Value
Planetary properties	
Radius (R)	$1.54 R_{\text{Jup,eq}}$
Gravity (g)	32.75 m s^{-2}
Rotation period (P_{rot})	2.65 Earth days
Thermodynamic quantities	
Specific heat capacity of H ₂ (c_{p,H_2})	$1.548 \times 10^4 \text{ J kg}^{-1} \text{ K}^{-1}$
Specific heat capacity of H ($c_{p,\text{H}}$)	$2.079 \times 10^4 \text{ J kg}^{-1} \text{ K}^{-1}$
Specific heat capacity of He ($c_{p,\text{He}}$)	$5193 \text{ J kg}^{-1} \text{ K}^{-1}$
He/H molar ratio ($x_{\text{He/H}}$)	0.0793
Specific gas constant of H ₂ (R_{H_2})	$4124 \text{ J kg}^{-1} \text{ K}^{-1}$
Specific gas constant of H (R_{H})	$8248 \text{ J kg}^{-1} \text{ K}^{-1}$
Specific gas constant of He (R_{He})	$2062 \text{ J kg}^{-1} \text{ K}^{-1}$
Specific recombination energy of H ₂ (L_{H})	$2.18 \times 10^8 \text{ J kg}^{-1}$
Radiative transfer parameters	
Irradiation temperature (T_{irr})	3348.85 K
Interior upward heat flux (T_{100})	3750 K
Minimum thermal opacity ($\kappa_{\text{R,min}}$)	$10^{-3} \text{ m}^2 \text{ kg}^{-1}$
Visible opacity scaling factor ($c_{\kappa,\text{vis}}$)	[1, 10]
Cloud opacity scaling factor ($c_{\kappa,\text{cld}}$)	[1, 10]
Cloud asymmetry parameter (g_{cld})	0.8
Cloud single scattering albedo ($\varpi_{0,\text{cld}}$)	0.95
Clear thermal photosphere ($p_{\text{phot,IR}}$)	142.5 mbar
Clear visible photosphere ($p_{\text{phot,vis}}$)	[251.3, 39.58] mbar
Cloud properties	
Condensate vapor deep mixing ratio (q_{deep})	$1.13 \times 10^{-4} \text{ kg kg}^{-1}$
Condensate vapor source pressure (p_{deep})	$5 \times 10^6 \text{ Pa}$
Condensate vapor deep relaxation timescale (τ_{deep})	10^3 s
Condensate density (ρ_c)	3950 kg m^{-3}
Mean particle size (r_0)	[2, 5] μm
Log-normal distribution width (σ)	1
Minimum particle bin radius (r_{min})	0.1 μm
Maximum particle bin radius (r_{max})	100 μm
Numerical parameters	
Drag timescale (τ_{drag})	10^7 s
Horizontal resolution	C48
Vertical resolution	70 layers
Lower boundary	100 bar
Upper boundary	10 μbar
Reference pressure (p_0)	1 bar
Shapiro filter order	4
Shapiro filter timescale	40 s
Dynamical time step	5 s, 10 s
Radiative time step	15 s, 30 s
H tracer relaxation timescale τ_{relax}	15 s
Condensate tracer relaxation timescale (τ_c)	15 s

Note. Brackets indicate parameter sensitivity tests over visible-band gas opacity, cloud opacity, and cloud particle size, while bold indicates baseline values for those parameters in our full suite of models.

The first two terms on the right-hand side of Equations (8) and (9) represent the source and sink of condensable vapor and cloud condensate, respectively. The final term on the right-hand

side of Equation (8) relaxes the condensible vapor mass mixing ratio at pressures higher than p_{deep} (here taken to be 50 bar; see Table 1) toward a deep source mixing ratio q_{deep} calculated assuming solar composition (Lodders 2003). As discussed further in Section 2.2.2, we assume that Al_2O_3 (corundum) is the dominant condensible species. We take the equilibrium condensation curve of corundum from Equation (4) of Wakeford et al. (2017). If the temperature is below the condensation temperature at any time and any location in the model, all local vapor is assumed to be supersaturated and therefore q_s is nearly zero; otherwise all condensates are relaxed back to vapor.

The final term on the right-hand side of Equation (9) represents the gravitational settling of cloud condensate at the terminal velocity V_p . Its form in altitude coordinates is

$$V_{\text{term}} = \frac{2\beta r^2 g(\rho_c - \rho)}{9\eta}, \quad (10)$$

where r is the cloud condensate particle size, ρ_c is the cloud condensate density, β is the Cunningham factor, which accounts for kinetic effects when the mean free path is larger than particle size, and η is the gas viscosity. We convert V_{term} in height coordinates to V_p in pressure coordinates assuming hydrostatic balance. As in Parmentier et al. (2013) and Komacek et al. (2019), we parameterize the Cunningham factor as a function of the Knudsen number Kn , the ratio of the mean free path to cloud particle size,

$$\text{Kn} = \frac{k_B T}{\sqrt{2} \pi r d^2 p}, \quad (11)$$

as

$$\beta = 1 + \text{Kn}(1.256 + 0.4e^{-1.1/\text{Kn}}), \quad (12)$$

and we parameterize the molecular viscosity as a function of the temperature as:

$$\eta = \frac{5}{16} \frac{\sqrt{\bar{m} k_B T}}{\sqrt{\pi} d^2} \frac{(k_B T / \epsilon)^{0.16}}{1.22}. \quad (13)$$

Symbols used in Equations (11)–(13) above include the Boltzmann constant k_B , the diameter of hydrogen gas $d = 2.827 \times 10^{-10}$ m, the mean molecular mass \bar{m} , and the depth of the H_2 potential well $\epsilon = 59.7 k_B$ K. The expressions in Equations (11)–(13) above are valid for temperatures ranging from 300 to 3000 K and at pressures less than 100 bar. As described below, condensate clouds do not form in high-temperature regions in our model. As a result, cloud settling is confined to relatively cool regions with a low mixing ratio of atomic hydrogen, ensuring that the condensation settling scheme above is a valid sink of cloud condensate in our GCM simulations.

As in Tan & Komacek (2019), we further couple the primitive equations to a tracer equation for the transport of the mass mixing ratio of atomic hydrogen relative to the total gas:

$$\frac{dq_H}{dt} = -\frac{\delta q_H}{\tau_{\text{relax}}}. \quad (14)$$

The change in the atomic hydrogen mass mixing ratio due to tracer transport δq_H is

$$\delta q_H = \frac{q_H - q_{H,\text{eq}}}{1 + \frac{L_H}{\bar{c}_p} \frac{\partial q_{H,\text{eq}}}{\partial T}}, \quad (15)$$

where the equilibrium mass mixing ratio of atomic hydrogen is $q_{H,\text{eq}}$ (see the following paragraph for further details). In the GCM, local changes in q_H affect the dynamics mainly through heating and cooling due to hydrogen recombination and dissociation, as expressed by the $\frac{\theta'}{\bar{c}_p T} \frac{L_H \delta q_H}{\tau_{\text{relax}}}$ term on the right-hand side of Equation (5). Other slightly minor dynamical effects include the change in the mean molecular weight and specific heat.

We improve upon the tracer scheme for atomic hydrogen from Tan & Komacek (2019) by incorporating the presence of helium in the mass budget. Given a molar fraction of atomic hydrogen relative to the total gas χ_H calculated from the Saha equation of the H_2 –H system (Berardo et al. 2017; Bell & Cowan 2018) and a prescribed molar ratio of helium to hydrogen $x_{\text{He}/\text{H}}$ (assumed to be Solar), we calculate the equilibrium mass mixing ratio of atomic hydrogen as

$$q_{H,\text{eq}} = \frac{\chi_H}{2 - \chi_H + 4x_{\text{He}/\text{H}}(2 - \chi_H)}. \quad (16)$$

This sets an upper limit on the equilibrium mass mixing ratio of atomic hydrogen of $q_{H,\text{max}} = 0.759$ if all of the hydrogen present at a given location is expected to be in atomic form. We also take into account helium gas in our formulation of the mean molecular weight and thus the mass-weighted specific gas constant and heat capacity:

$$\bar{R} = R_H q_H + R_{\text{H}_2}(q_{H,\text{max}} - q_H) + R_{\text{He}}(1 - q_{H,\text{max}}), \quad (17)$$

$$\bar{c}_p = c_{p,\text{H}} q_H + c_{p,\text{H}_2}(q_{H,\text{max}} - q_H) + c_{p,\text{He}}(1 - q_{H,\text{max}}). \quad (18)$$

Our assumed values for specific heat capacity and gas constant of each component of the atmosphere (H, H_2 , He) are shown in Table 1. Note that our choices of the specific heat capacity for each component result in an average $c_p = 13,000 \text{ J kg}^{-1} \text{ K}^{-1}$ at low temperature (i.e., with $q_H = 0$), consistent with that used in previous MITgcm simulations of the atmospheric dynamics of hot and ultra-hot Jupiters (e.g., Showman et al. 2009; Liu & Showman 2013; Kataria et al. 2013; Tan & Komacek 2019; Steinrueck et al. 2021). Though the inclusion of inert helium gas reduces the thermodynamic effect of hydrogen dissociation and recombination, we show in Section 4.1 that the thermal impact of hydrogen dissociation and recombination has a strong effect on the thermal structure predicted by our GCMs.

As in Tan & Komacek (2019) and May et al. (2021), we couple a modified version of the DISORT TWOSTR plane-parallel two-stream double-gray radiative transfer scheme with the multiple scattering approximation (Stamnes et al. 1988; Kylling et al. 1995) to our dynamical core. Gas opacities are considered to be purely absorptive, but cloud opacities include multiple scattering. We set the visible and infrared background gas opacities to be functions of pressure alone, with the gas opacity in the visible band parameterized as

$$\kappa_{g,\text{vis}} = 10^{0.0478(\log_{10} p[\text{Pa}])^2 - 0.1366(\log_{10} p[\text{Pa}]) - 3.2095} \text{ m}^2 \text{ kg}^{-1}, \quad (19)$$

and the gas opacity in the infrared band set to

$$\kappa_{g,IR} = \max(10^{0.0498(\log_{10}P[\text{Pa}])^2 - 0.1329(\log_{10}P[\text{Pa}]) - 2.9457}, 10^{-3}) \text{ m}^2 \text{ kg}^{-1}. \quad (20)$$

As in May et al. (2021) and Tan & Showman (2021a, 2021b), we include a constant minimal opacity given that the use of a Rosseland-mean opacity in the double-gray framework would otherwise cause low pressures in the model to become optically thin and radiatively inactive, where in reality narrow absorption bands drive radiative heating/cooling. We choose a minimal opacity κ_{\min} of $10^{-3} \text{ m}^2 \text{ kg}^{-1}$, consistent with the thermal opacity used in previous double-gray models of hot Jupiter atmospheres (Guillot 2010). To incorporate the current evolutionary state of TOI-1431b modeled in Section 2.1, as in May et al. (2021) we prescribe a “surface” temperature of 3750 K at 100 bar in our radiative transfer scheme. Our simulations do not include a dry convective adjustment scheme due to the inclusion of hydrogen dissociation and recombination, which enforces the lapse rate to be smaller than the lapse rate of H_2 alone. As a result, the thermal structure is not prescribed at any atmospheric level, and instead is controlled by dynamics and radiative transfer.

We include the cloud opacity as follows. We calculate the cloud extinction opacity by scaling from the gas opacity in both the visible and thermal band as

$$\begin{aligned} \kappa_{c,vis} &= \frac{q_c}{q_{\text{deep}}} c_{\kappa,\text{cld}} \kappa_{g,vis}, \\ \kappa_{c,IR} &= \frac{q_c}{q_{\text{deep}}} c_{\kappa,\text{cld}} \kappa_{g,IR}, \end{aligned} \quad (21)$$

where $c_{\kappa,\text{cld}}$ is a scaling factor for the cloud extinction opacity relative to the gas opacity in both the visible and thermal bands. Here, q_{deep} is a fixed parameter in each simulation, and the local cloud opacity depends on the time-dependent and spatially inhomogeneous distribution of clouds that are coupled to the dynamics. From CARMA microphysics simulations as described below, clouds on the nightside of hot Jupiters are usually optically thick and highly scattering. We prescribe a fixed cloud asymmetry parameter (g_{cld}) and single scattering albedo ($\varpi_{0,\text{cld}}$) to determine the cloud optical properties, discussed further in Section 2.2.2. These assumed cloud optical properties are used in both the double-gray multiple scattering radiative transfer scheme in the GCM along with the `gCMCRT` code used in post-processing.

Note that our cloud extinction opacity has the same scaling to the gas opacity in both the visible and optical bands. This simplification is justified in the regime of ultra-hot Jupiters due to the lack of significant cloud mass on the dayside and thus a minimal cloud-radiative effect in the visible wavelength band. There are other schemes to parameterize cloud opacity in semi-gray GCMs of hot Jupiters and brown dwarfs (e.g., Roman et al. 2021; Tan & Showman 2021b) that specify the cloud particle size or number density. Our current method is simpler and provides a clear setup to understand how the atmospheric circulation and cloud structure are affected by the radiative effect of clouds.

The total atmospheric opacity at a given layer for each wavelength band is simply set by a weighted sum of the gas

and cloud opacities,

$$\begin{aligned} \kappa_{vis} &= c_{\kappa,vis} \kappa_{g,vis} + \kappa_{c,vis}, \\ \kappa_{IR} &= \kappa_{g,IR} + \kappa_{c,IR}. \end{aligned} \quad (22)$$

We include an additional scaling factor for the visible-band gas opacity ($c_{\kappa,vis}$) in order to mimic the effects of visible absorbers (e.g., atomic metal species) on the temperature structure by considering an increased visible-band opacity. We formulate the total opacity in each band in this manner in order to have only two free radiative transfer parameters in our model suite: $c_{\kappa,vis}$ and $c_{\kappa,\text{cld}}$. Our two-stream, double-gray radiative transfer scheme including cloud extinction and scattering is then coupled to the dynamical core through the vertical divergence of net radiative flux leading to heating and cooling, as shown by the term $\frac{g\theta'}{c_p T} \frac{\partial F}{\partial p}$ on the right-hand side of Equation (5).

2.2.2. Cloud Microphysical and Radiative Properties

We parameterize cloud microphysical and radiative properties in our GCM using predicted cloud particle size distributions and optical properties from the CARMA cloud microphysical simulations of Gao & Powell (2021). CARMA has been recently applied to study the cloud microphysics of hot Jupiters by Powell et al. (2018), Powell et al. (2019), Gao et al. (2020), Gao & Powell (2021), and it models a range of microphysical processes including heterogeneous and homogeneous nucleation, condensational growth and evaporation, coagulation, and vertical lofting and settling (see Appendix A of Gao et al. (2018) for details).

Specifically, we utilize the cloud microphysical and optical properties from the $T_{\text{eq}} = 2100 \text{ K}$ model of Gao & Powell (2021), which considers the heterogeneous nucleation of a variety of species, most notably forsterite (Mg_2SiO_4) and corundum (Al_2O_3), on titanium dioxide (TiO_2) grains, along with the homogeneous nucleation of TiO_2 and Fe, among other species. The resulting cloud particle size distribution for each condensate species from these CARMA simulations is roughly log-normal, with characteristic particle sizes ranging from ~ 1 to $10 \mu\text{m}$. As a result, we parameterize a log-normal cloud particle size distribution in our GCM as

$$\frac{dn_c}{dr} = \frac{n_c}{\sqrt{2\pi}\sigma r} e^{-[\ln(r/r_0)]^2 / (2\sigma^2)}, \quad (23)$$

where n_c is the cloud particle number per dry air mass, r_0 is the mean particle size, σ is the log-normal distribution width, and n_c is the number of cloud particles per dry air mass, calculated as

$$n_c = \frac{3q_c}{4\pi\rho_c r_0^3 e^{(4.5\sigma^2)}}. \quad (24)$$

Given that our cloud optical properties are set to a fixed value independent of particle size (see below), our assumed cloud particle size distribution only impacts the vertical settling of particles through the sink term for cloud condensate on the right-hand side of Equation (9), $-\frac{\partial(q_c \langle V_p \rangle)}{\partial p}$, in which the mean terminal velocity is obtained from proper averaging over the size distribution in Equation (23).

In this work, we include a single cloud condensate tracer along with a single tracer for condensable vapor, using cloud condensate and condensable vapor properties appropriate for

Table 2

List of GCM Simulations Conducted for This Work, Along with The Parameters Modified from The Baseline Model for Each Case

Simulation ID	Parameter modifications
Baseline	None
No cloud RT	Radiatively inactive clouds
Reduced cloud opacity (Red. κ_{cld})	$c_{\kappa,\text{cld}} = 1$
Reduced cloud particle size (Red. r_0)	$r_0 = 2\mu\text{m}$
Enhanced visible opacity (Enh. κ_{vis})	$c_{\kappa,\text{vis}} = 10$

Note. We conduct five GCM simulations in total in order to study the effect of varying the properties and existence of cloud-radiative feedback and of varying the visible-to-infrared gas opacity ratio (i.e., $\kappa_{\text{g,vis}}/\kappa_{\text{g,IR}}$; Guillot 2010) on the atmospheric dynamics of ultra-hot Jupiters.

corundum. We isolate the local condensation and transport of corundum in this work because it is the highest-temperature condensate expected to contribute significantly to the cloud opacity of ultra-hot Jupiters (Gao & Powell 2021). As a result, by considering corundum condensation alone in this work we constrain how dynamics, cloud tracer transport, and cloud-radiative feedback set the greatest possible extent of the cloud deck on ultra-hot Jupiters. We assume the density of corundum clouds from Roman et al. (2021), and take the condensation temperature and deep condensible vapor mixing ratio appropriate for corundum from Wakeford et al. (2017) and Lodders (2003). We choose baseline cloud optical properties, including the cloud asymmetry parameter, single scattering albedo, and cloud opacity scaling factor, from their characteristic values in the near-infrared at the 10–100 mbar level in the $T_{\text{eq}} = 2100$ K CARMA simulation of Gao & Powell (2021) where there is a thick corundum cloud deck in the model. The cloud single scattering albedo and asymmetry parameter are unchanged throughout the suite of GCMs conducted here, and instead the only free parameter that directly affects the cloud-radiative feedback is the cloud opacity scaling factor $c_{\kappa,\text{cld}}$. Table 1 shows all of our parameter choices in the model, with free parameters expressed in brackets and their baseline value in bold face.

2.2.3. Suite of GCMs with Cloud Tracers

We conduct a suite of GCMs modifying three free parameters individually: the cloud opacity scaling factor $c_{\kappa,\text{cld}}$, the visible gas opacity scaling factor $c_{\kappa,\text{vis}}$, and the mean cloud particle size r_0 . We additionally conduct a simulation with the cloud-radiative feedback turned off, resulting in no cloud extinction or scattering in the radiative transfer module. Along with our baseline case with radiatively active clouds, this results in a total of five GCMs in our main model suite. Table 2 shows the simulation identification and parameter modification from the baseline case for each simulation in our GCM suite.

Each GCM in our model suite has a cubed-sphere resolution of C48, approximately equivalent to a horizontal resolution of 192×96 in longitude and latitude. Each GCM uses 70 vertical layers, spaced logarithmically in pressure from 100 bar to 10 μbar . We take planetary parameters (radius, gravity, rotation period, irradiation temperature) appropriate for TOI-1431b from Addison et al. (2021). We use a weak height-independent frictional drag in all simulations, characterized by a drag timescale $\tau_{\text{drag}} = 10^7$ s. This weak drag ensures that our simulations reach an equilibrated end-state, and Komacek &

Showman (2016) and Komacek et al. (2017) have previously shown that varying the drag timescale from 10^7 s to ∞ does not significantly affect the resulting flow structure. The GCM further includes a fourth-order Shapiro filter in order to prevent subgrid scale momentum buildup without qualitatively affecting the large-scale flow. Our standard time step in the dynamical core is 10 s, with the radiative time step set equal to three times the dynamical time step. In the case with an enhanced visible opacity ($c_{\kappa,\text{vis}} = 10$), we reduce the dynamical time step to 5 s for numerical stability. We set the hydrogen and condensation tracer relaxation timescale $\tau_{\text{relax}} = \tau_{\text{c}} = 15$ s, slightly larger than a dynamical time step. Each simulation is initialized from rest with an isothermal temperature profile of $T = 2368$ K. Each case is then continued to at least 2500 Earth days, after which we confirm that each GCM simulation has reached an equilibrated state in both the domain-integrated kinetic and thermal energy.⁷ As expected from previous studies of the atmospheric dynamics of hot Jupiters (Menou et al. 2003; Rauscher et al. 2007; Dobbs-Dixon et al. 2010; Komacek & Showman 2020; Cho et al. 2021), our simulations display time-variability in the temperature, winds, and cloud mass mixing ratio. However, in this work we focus on the impact of clouds on the climate of ultra-hot Jupiters, and leave more detailed studies of meteorology to future work. As a result, all GCM results shown are time averages over the final 500 Earth days of simulated time.

3. Results

3.1. Atmospheric Dynamics and Cloud Coverage

3.1.1. Baseline Case

Before comparing models with varying cloud microphysical and radiative assumptions, we first study the emergent behavior in our baseline model with radiatively active clouds. Figure 2 shows the temperature and wind patterns along with the atomic hydrogen mixing ratio and cloud coverage from the baseline model on isobars ranging from 1 bar to 10 μbar . Note that the temperature, wind, atomic hydrogen mixing ratio, and cloud coverage maps on isobars from the entire suite of GCMs are shown in Appendix A.1.

The temperature and wind patterns near the infrared photosphere (which lies at a pressure of 142.5 mbar; see Table 1) in the baseline case are similar to those expected from the broad range of previous studies of hot and ultra-hot Jupiters (Heng & Showman 2015; Showman et al. 2020). At these pressures, the atmosphere is characterized by a large day-to-night temperature contrast (Perna et al. 2012; Perez-Becker & Showman 2013; Komacek & Showman 2016) that triggers a planetary-scale equatorial wave pattern (Showman & Polvani 2011; Showman et al. 2013; Tsai et al. 2014; Hammond & Pierrehumbert 2018; Penn & Vallis 2018; Pierrehumbert & Hammond 2019; Hammond & Lewis 2021). The superposition of mid-latitude westward shifted Rossby modes and equatorially trapped eastward Kelvin modes leads to phase tilts that act to pump momentum toward the equator, causing a

⁷ Note that this may be only the first time at which the model would reach kinetic and thermal energy “equilibrium,” as long-timescale (tens to hundreds of thousands of Earth day) integrations of gas giant and sub-Neptune GCMs have found significant time evolution in both the domain-integrated energetics and qualitative predictions for atmospheric dynamics (Mayne et al. 2017; Sainsbury-Martinez et al. 2019; Young et al. 2019; Mendonca 2020; Wang & Wordsworth 2020; Schneider et al. 2022).

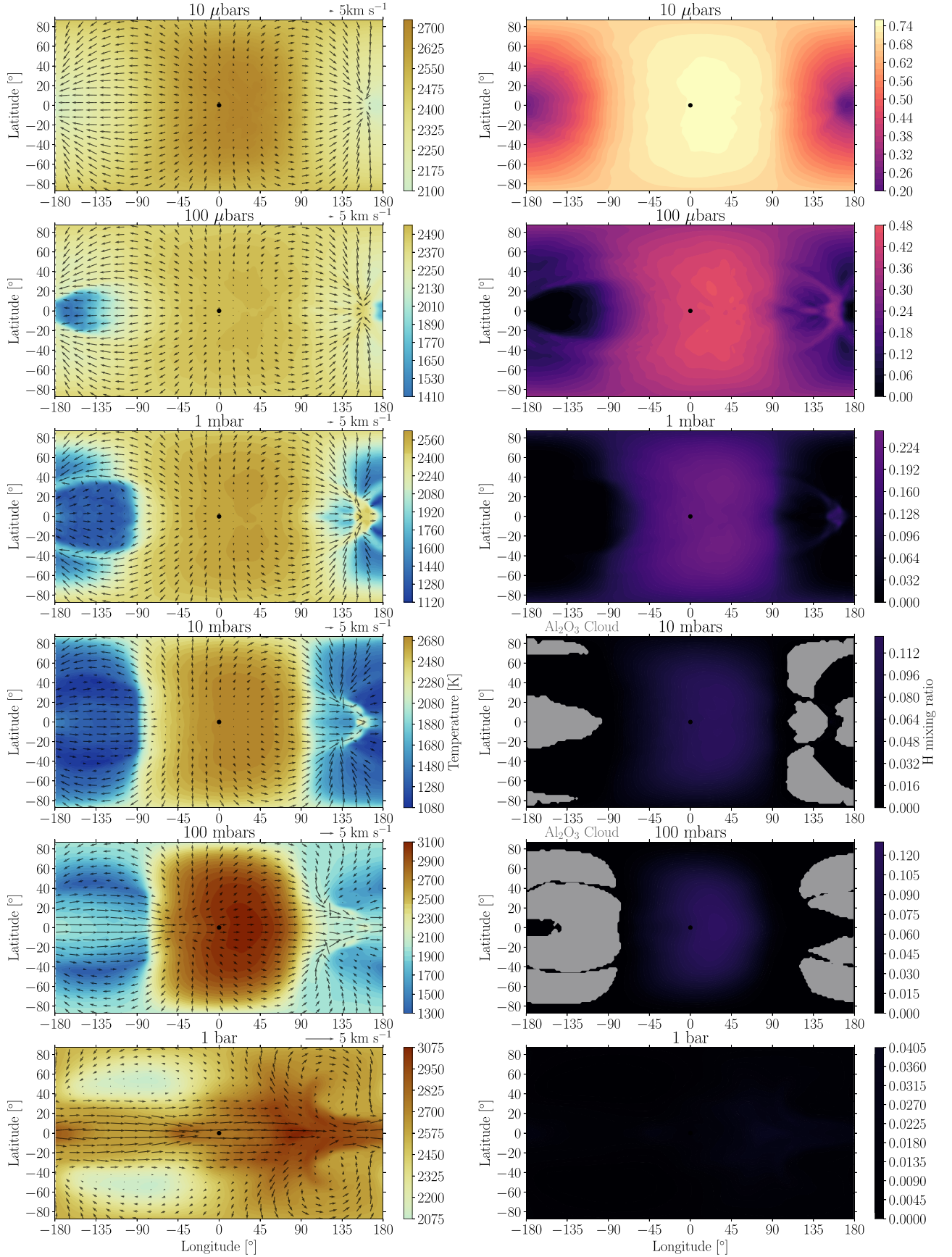


Figure 2. Temperature maps with overlaid wind arrows (left) and atomic hydrogen mass mixing ratio (right, colors) with overlaid cloud tracer distributions (gray regions show where the cloud mass mixing ratio is $\geq 5 \times 10^{-5}$ kg kg $^{-1}$) plotted on isobars logarithmically spaced from 10 μ bar to 1 bar from the baseline GCM simulation with radiatively active cloud tracers. All panels in each respective column share a color scale. The upper atmosphere has significant atomic hydrogen on the dayside, and hydrogen on the nightside is fully recombined at pressures \gg 1 mbar. Patchy clouds occur on the nightside at pressures of 10 and 100 mbar.

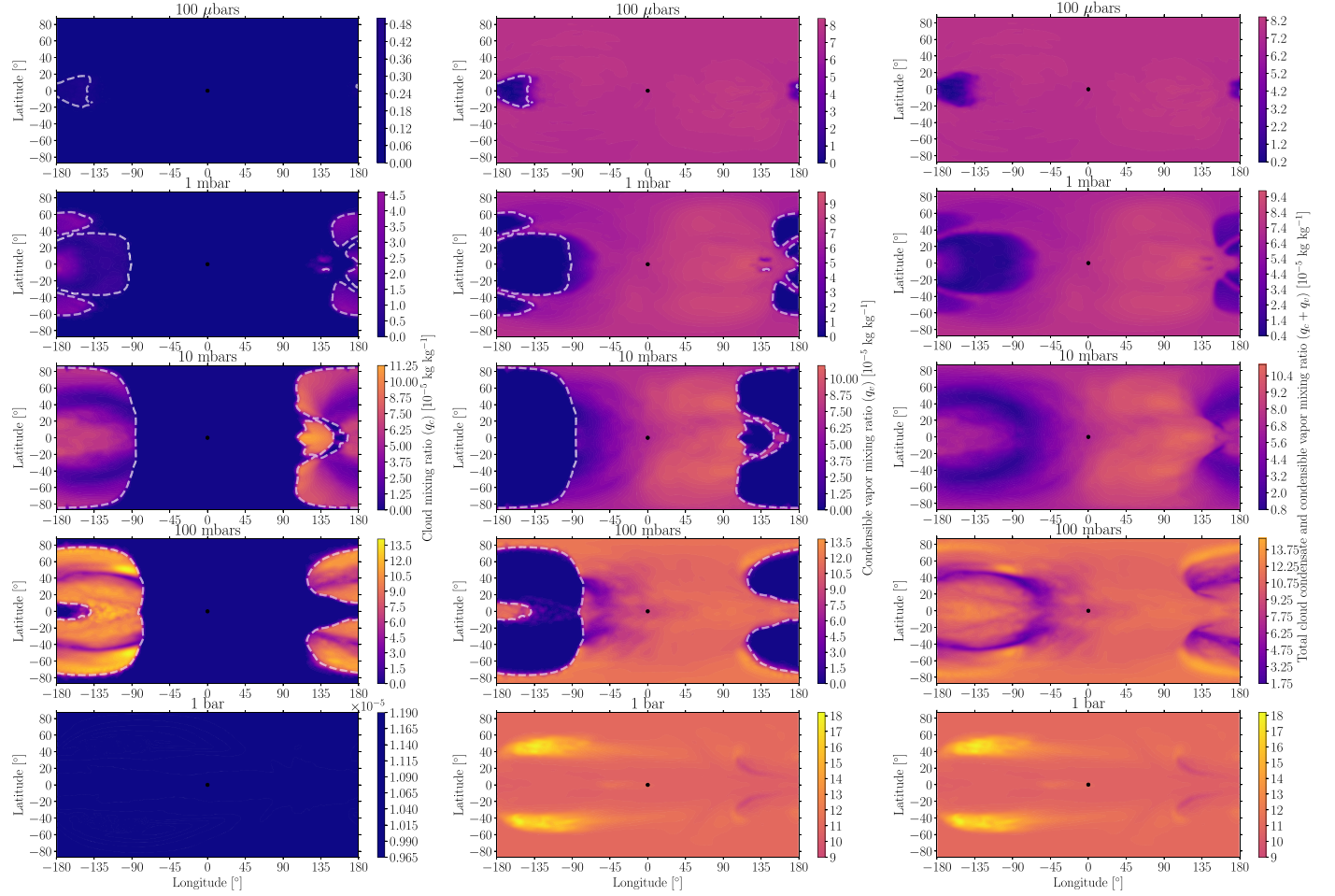


Figure 3. Maps of the cloud condensate and condensable vapor tracer distribution from our baseline GCM simulation with radiatively active cloud tracers. Shown are the cloud mass mixing ratio (left), condensable vapor mass mixing ratio (middle), and the sum of cloud and condensable vapor mass mixing ratio (right) on isobars logarithmically spaced from 100 μ bar to 1 bar. All panels in a given column share a color scale, and all mass mixing ratios are shown in units of 10^{-5} . The snow-white dashed contour in the cloud and condensable vapor maps displays where the gas temperature is equal to the corundum condensation temperature on each isobar. Patchy clouds form on the nightside and western limb, but are confined between pressure levels of \sim mbar to a bar. The cloud mass mixing ratio is the largest in the mid-latitudes at the 100 mbar level.

superrotating equatorial jet shown by the eastward direction of winds throughout the equatorial region (Showman & Polvani 2011) at pressures ≥ 10 mbar in Figure 2. This superrotating equatorial jet then Doppler shifts the planetary-scale wave pattern, leading to an eastward hot spot offset due to the eastward shift of the equatorially trapped Kelvin wave component (Penn & Vallis 2017; Hammond & Pierrehumbert 2018). The Rossby wave component of the planetary-scale wave pattern induces cyclonic motions (“Rossby gyres”) poleward of the mid-latitude flanks of the equatorial jet on the nightside (Cho et al. 2021). Relevant for cloud condensation, the coldest regions in the simulation occur at the intersection of the equatorial jet and Rossby gyres, at which convergence induces a narrow band of cold downwelling air in the mid-latitudes.

The atmospheric circulation at pressures ≤ 1 mbar is markedly different than that at higher pressures. This is because the radiative timescale scales linearly with the overlying column mass of atmosphere and thus the pressure itself (Showman & Guillot 2002). The short radiative timescale at low pressures leads to strong radiative damping of the planetary-scale wave pattern, preventing the equatorward momentum transport required to sustain the equatorial jet (Showman et al. 2013).

As a result, the circulation at low pressures is characterized by substellar-to-anti-stellar flow, rather than a superrotating equatorial jet and Rossby gyres as for higher pressures. Low pressures also promote the dissociation of molecular hydrogen (Bell & Cowan 2018), leading to an increase in the mass mixing ratio of atomic hydrogen on the dayside with decreasing pressure. As we display further in Section 3.1.4 and demonstrate in Section 4.1, the increased atomic hydrogen mass mixing ratio at low pressures on the dayside leads to a thermodynamically induced thermal inversion on the nightside due to the heat release during the recombination of atomic to molecular hydrogen. This causes a decrease in the day-to-night temperature contrast at the lowest pressures in the model domain relative to the day–night contrasts near the infrared photosphere.

The regions with significant corundum condensate cloud coverage are shown by the gray area on the right-hand column of Figure 2. Clouds with a local mass mixing ratio $\geq 5 \times 10^{-5}$ kg kg only persist at pressure levels between 10 and 100 mbar in this baseline simulation. Figure 3 shows maps of the cloud and vapor mass mixing ratios from the baseline case with radiatively active cloud tracers, which display that significant cloud mass does persist to the 1 mbar level. Note that

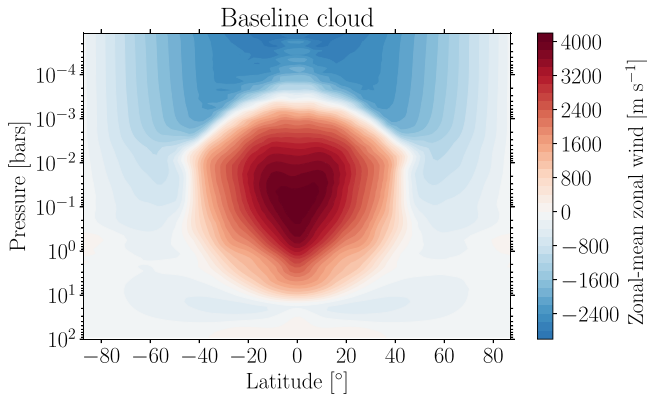


Figure 4. Zonal-mean zonal wind from the baseline GCM simulation with active cloud tracers. There is a superrotating equatorial jet at pressures $\gtrsim 1$ mbar that extends to the ~ 10 bar level along with a transition from superrotation to subrotation with decreasing pressure.

Appendix A.2 shows maps of cloud and vapor mass mixing ratio from the suite of models with varying cloud microphysical and radiative properties. As discussed in Section 3.1.2, we do not find significant cloud coverage at pressures $\ll 1$ mbar in any case in our model suite, as there is a decrease of almost 2 orders of magnitude in cloud mass mixing ratio from the peak at 100 mbar to the 100 μ bar level. We further find that the cloud distribution is inherently nonuniform in both the horizontal and vertical directions. We find that the dayside is generally cloud-free, except for a thin region at depth near the western terminator. The cloud coverage on the nightside is patchy, with a maximum in cloud mass mixing ratio at the 100 mbar level in the mid-latitudes and local minima in cloud mass mixing ratio at latitudes of $\approx 40^\circ$ and at localized regions near the equator.

Notably, the cloud coverage does not align solely with the atmospheric temperature structure—the coldest regions at 10 and 100 mbar are not uniformly cloudy. This is especially true for the regions on the mid-latitude nightside where there is a transition from the eastward superrotating jet at lower latitudes to cyclonic flow in the Rossby gyres at higher latitudes. As we will demonstrate in Section 3.1.3, this is due to the dependence of vertical mixing on the correlation between the vertical velocity and cloud tracer distribution (Holton 1986; Zhang & Showman 2018a, 2018b). The convergence between the superrotating jet and Rossby gyres implies downwelling motions through mass continuity in the primitive equations of motion (Equation (4); see also Holton & Hakim 2013 and Vallis 2017), which then causes net downward transport of cloud tracers. Cloud tracers are then either advected into upwelling regions or converted into vapor at the warmer higher pressure levels.

Figure 4 shows the zonal-mean zonal wind (east–west average of the east–west wind) from our baseline case with active cloud tracers. Note that the zonal-mean zonal wind speeds for the remaining cases in our model suite are shown in Appendix A.3. In the baseline case, we find a maximum zonal-mean zonal wind speed just above 4 km s^{-1} . As demonstrated in Tan & Komacek (2019), this maximum wind speed is smaller than in equivalent cases without the thermodynamic effect of hydrogen dissociation and recombination due to the muted planetary-scale wave pattern.

Similar to the high-temperature cases with a fixed rotation period of 2.43 Earth days (close to our assumed rotation period

of 2.65 Earth days) in Tan & Komacek (2019), we further find that the direction of the zonal-mean equatorial flow, \bar{u} , reverses from superrotating (eastward) to subrotating (westward) with decreasing pressure. This reversal coincides with the transition between superrotation and day-to-night flow shown in Figure 2. It also coincides with pressures at which atomic hydrogen persists on the nightside, causing direct thermodynamic effects on the atmospheric circulation. The thermodynamic impact of hydrogen dissociation and recombination along with the strong radiative cooling at low pressures combine to disrupt the planetary-scale equatorial wave pattern and thus the wave-mean flow interactions that drive the equatorial jet, preventing the superrotating equatorial jet from extending to lower pressures.

Additional insights of this vertical flow reversal come from the thermal wind balance, whose form at low latitudes can be written as (e.g., Holton & Hakim 2013, Chapter 12.6):

$$\frac{\partial \bar{u}}{\partial \ln p} = \frac{1}{\beta} \frac{\partial^2 \bar{T}}{\partial y^2} = \frac{R_{\text{H}_2}}{\beta} \times \frac{\partial^2 \left[\frac{R_{\text{H}}}{R_{\text{H}_2}} q_{\text{H}} + (q_{\text{H,max}} - q_{\text{H}}) + \frac{R_{\text{He}}}{R_{\text{H}_2}} (1 - q_{\text{H,max}}) \right] T}{\partial y^2}, \quad (25)$$

where y is distance that increases northward, $\beta = df/dy$ is the meridional gradient of the Coriolis parameter f at the equator, and \bar{A} denotes the zonal mean of the quantity A . The horizontal wind patterns at low pressures preferentially transport atomic H from the dayside deeply into the nightside at high latitudes but less so from the equator. Meanwhile, low latitudes on the nightside are colder and have more H_2 than high latitudes at low pressures (see Figure 2). By thermal wind balance as in Equation (25), both the meridional temperature and composition gradient at low pressures favor a strong positive $\partial \bar{u} / \partial \ln p$, giving rise to the flow reversal seen in Figure 4. Note that we do not imply that the thermal wind balance fully holds on slowly rotating hot Jupiters. In the weak frictional drag regime, the horizontal force balance on hot Jupiters is expected to be set by a combination of the pressure gradient force, Coriolis force, and the nonlinear advection term (Showman et al. 2013). However, the strong equator-to-pole thermal and compositional gradients at low pressures still place an important constraint on the vertical shear of the zonal-mean flow.

3.1.2. Cloud Coverage

In all cases with cloud condensation, we find that the cloud coverage in the atmosphere of our simulated ultra-hot Jupiter is patchy, being both horizontally and vertically nonuniform. Figure 5 shows the meridional-mean condensate cloud tracer mass mixing ratio on isobars from 1 bar to 0.1 mbar as a function of the longitude for four simulations: the baseline case, the case without cloud-radiative feedback, the case with reduced cloud opacity, and the case with a reduced characteristic cloud particle size. Results are not shown from the case with an enhanced visible opacity because only a small mass of condensate cloud persists at depth. We find that in the cases with cloud condensation, clouds only form near the western limb and on the nightside. Further, clouds are sequestered at depth, with no cloud condensate persisting at pressures

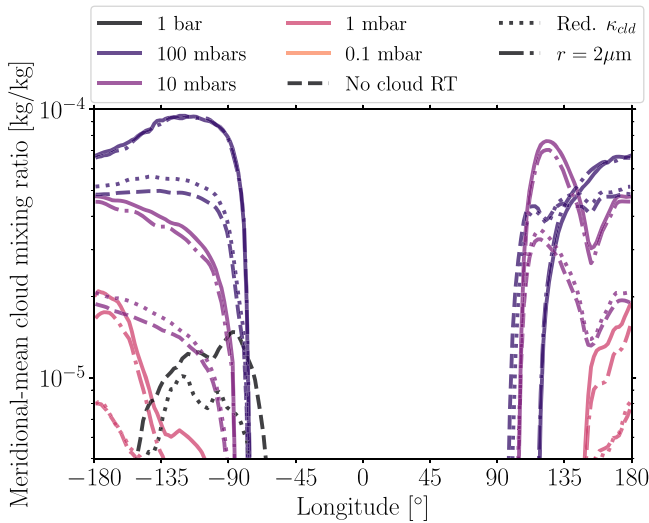


Figure 5. Meridional mean of cloud mass mixing ratio as a function of the longitude at different pressures from GCM simulations with varying cloud assumptions. Clouds are largely confined to pressures $\gtrsim 10$ mbar on the western limb and to $\gtrsim 1$ mbar on the nightside. Though the western terminator is cloudy at 100 mbar in all cases, the eastern terminator is always cloud-free. There are no clouds at 0.1 mbar with a mass mixing ratio $\gtrsim 10^{-6}$ kg kg $^{-1}$. Clouds form at high pressures of 1 bar only in the case without cloud-radiative feedback, as otherwise the cloud greenhouse effect warms the deep atmosphere, preventing cloud condensation at depth.

significantly less than 1 mbar on the nightside and western limb. The cloud decks are further prevented from extending to depth, as they only persist to the 1 bar level in the cases without significant cloud-radiative feedback. As described in Section 3.1.4, cloud-radiative feedback leads to a cloud greenhouse effect that acts to warm the atmosphere at higher pressures than the cloud deck, preventing cloud condensation at depth.

In all models considered, we find that clouds are sequestered between isobars of approximately 1 bar and several hundreds of μ bar. Figure 6 shows pressure profiles of the meridional-mean cloud mass mixing ratio and infrared cloud extinction opacity at the anti-stellar point, west limb, and on a global average in the four cases where cloud condensate forms. Note that no significant cloud mass forms at the substellar point or east limb for any of our assumed cloud microphysical and radiative properties. The pressure range over which the cloud deck extends depends on both the longitude at which the cloud deck forms and assumptions about cloud-radiative properties. In all cases, the cloud top occurs at a lower pressure on the anti-stellar point than at the western limb. The cloud top also occurs at lower pressures in cases that include a strong cloud-radiative feedback (i.e., the baseline and reduced cloud particle size cases) relative to those with a weak (reduced cloud opacity) or zero cloud-radiative feedback, both at the anti-stellar point and western limb individually and on a global average. This is due to the radiative feedback of the cloud deck on the thermal structure, as the cloud greenhouse effect warms the underlying atmosphere, causing the cloud deck to move to lower pressures in cases with a strong cloud-radiative feedback. However, the cloud extinction opacity is much smaller than the gas opacity at low pressures $\ll 1$ mbar. Near the base of the cloud deck, the cloud extinction opacity on the nightside and western limb can be larger than the infrared gas opacity alone. As we discuss in Section 3.2, this implies that clouds have a minor impact on transmission spectroscopy but a significant impact on nightside

emission and phase curve observations in the cases considered here.

3.1.3. Vertical Mixing

To study how the vertical mixing of cloud tracer sets the patchy cloud distribution, we calculate the vertical mixing efficiency from our suite of models. The mixing efficiency is defined as (Parmentier et al. 2013):

$$F = \frac{\omega(q - \langle q \rangle)}{\langle \omega q \rangle}. \quad (26)$$

In Equation (26), ω is the vertical velocity in pressure coordinates ($\omega = dp/dt$), q is the tracer mass mixing ratio (of cloud condensate and/or condensible vapor), and brackets represent the mean on an isobar. Note that the actual mixing efficiency could be higher than that estimated in our GCM framework due to turbulence generated by shear instabilities (Menou 2019, 2021). The mixing efficiency encapsulates a key property of tracer mixing: net vertical transport of tracer across isobars can only occur at locations where there is a correlation between the tracer abundance and the vertical velocity (for a schematic depiction, see Figure 2 of Zhang & Showman (2018a)). In Equation (26), the numerator $\omega(q - \langle q \rangle)$ represents this correlation between vertical velocity and tracer mixing ratio, as a net upward vertical transport of tracer will occur if $\omega(q - \langle q \rangle) < 0$, and a net downward vertical transport will occur if $\omega(q - \langle q \rangle) > 0$ locally⁸. The denominator in Equation (26) ($\langle \omega q \rangle$) is related to the mean upward flux of material across isobars, and normalizes the mixing efficiency F such that it represents the local contribution to the total upward flux on an isobar.

Positive mixing efficiency thus corresponds to net upward tracer transport on an isobar, and negative mixing efficiency corresponds to net downward tracer transport on an isobar. Importantly, local positive mixing efficiency can correspond to one of two possibilities: upward winds are transporting air enhanced in tracer across isobars *or* downward winds are transporting air depleted in tracer across isobars. Both of these scenarios create the correlation between vertical velocity and tracer mixing ratio required for net upward tracer transport. For net downward tracer transport, which corresponds to negative mixing efficiency, the opposite is true: either downward winds are transporting air enhanced in tracer across isobars, or upward winds are transporting air depleted in tracer across isobars.

We define two separate mixing efficiencies: a “cloud mixing efficiency” (F_c) for the cloud condensate alone, with $q = q_c$ in Equation (26), and a “total mixing efficiency” (F_{tot}) for the total tracer including both cloud condensate and condensible vapor, with $q = q_c + q_v$ in Equation (26). We do so because though the cloud mixing efficiency represents the vertical mixing of cloud species, this is affected by the inhomogeneous temperature structure, most notably the large day-to-night contrast that prevents cloud condensation throughout much of the dayside. Meanwhile, the total mixing efficiency more closely displays the direct effect of transport on tracer mixing.

The mixing efficiencies at pressure levels of 1 mbar, 10 mbar, and 100 mbar from our baseline case with radiatively

⁸ Note the reversed sign from standard vertical velocity with dimensions of length rather than pressure.

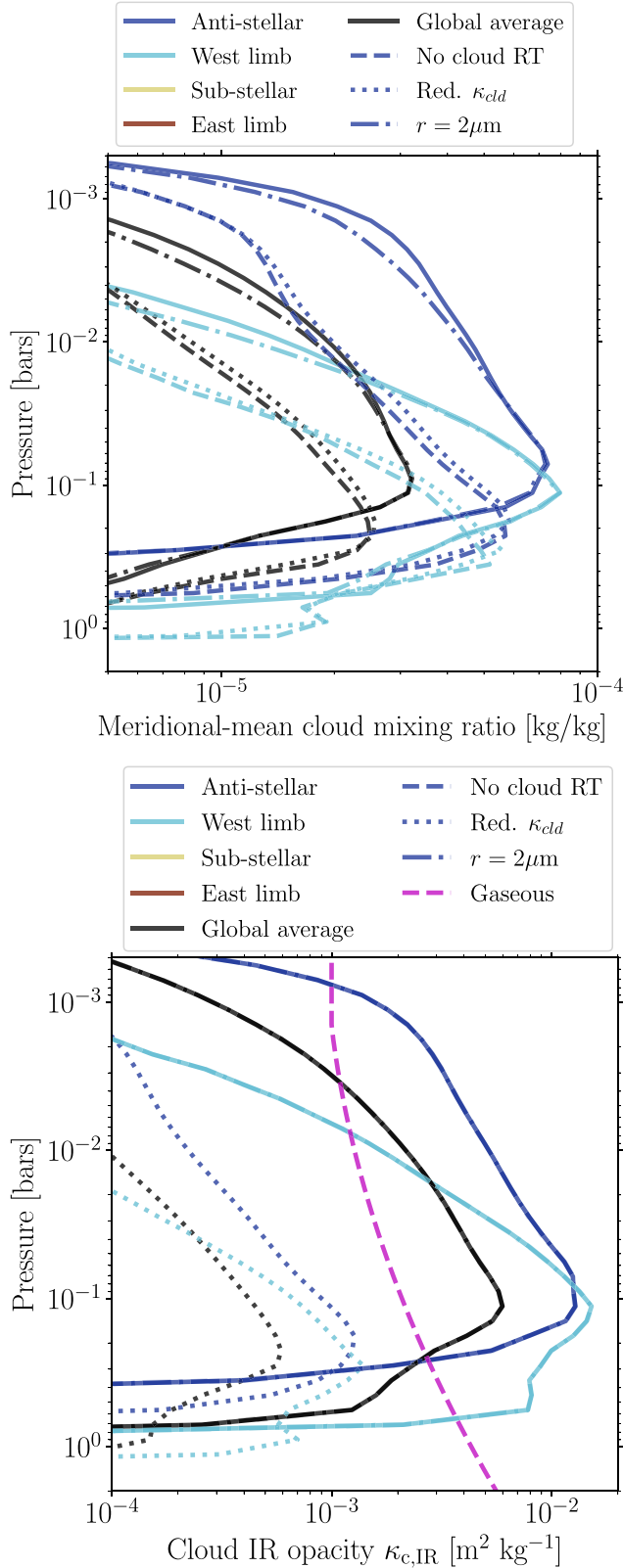


Figure 6. Top: Vertical profiles of the meridional mean of cloud mixing ratio at various longitudes (colors) and the respective global horizontal mean (black lines) from GCM simulations with varying cloud assumptions. Bottom: Vertical profiles of the corresponding IR cloud extinction opacity. There is no significant cloud mass and resulting opacity at any pressure at the substellar point or eastern limb. We find that the cloud-top pressure is lower in cases with higher cloud extinction opacity and resulting stronger cloud-radiative feedback. Clouds on the nightside and western limb are sequestered at depth, with the cloud opacity much smaller than the gas opacity at pressures $\ll 1$ mbar.

active cloud tracers is shown in Figure 7 along with vertical pressure velocity contours on the same isobars. Additionally, the vertical velocities and mixing efficiencies at the 100 mbar isobar from cases with varying cloud microphysical and radiative assumptions are further shown in Appendix A.4. Note that the mixing efficiency is not undefined in any of these locations, given that all pressures considered have at least a minuscule amount of cloud and condensable vapor tracer present in the numerical scheme. We find that there is strong spatial inhomogeneity in the pattern of both the cloud and total mixing efficiency on the nightside and limbs, which drives the emergent patchy cloud behavior. At the equator, local changes in mixing efficiency generally correspond to changes in the speed of the equatorial jet, which drives convergence or divergence that causes downwelling or upwelling, respectively (Parmentier et al. 2013). The eastward flow near the equator causes a horizontal asymmetry in the background vapor (with more condensable vapor eastward of the substellar point; see Figure 3), which at pressures of 10–100 mbar causes net total tracer lofting (i.e., positive total mixing efficiency) eastward of the substellar point and net tracer settling westward of the substellar point. One specific region with strong variations in both cloud and total mixing efficiency is the descending region eastward of the eastern terminator where the equatorial jet slows, which has been shown to lead to local adiabatic warming in previous simulations of ultra-hot Jupiters (Beltz et al. 2022). The downward vertical velocity in this region and resulting negative mixing efficiency at 100 mbar transports cloud condensate downward and causes a local minimum in cloud mixing ratio on the nightside that at 100 mbar can extend eastward of the anti-stellar point.

Figure 7 shows that along with the variations in mixing along the equator, there are also significant changes in vertical pressure velocity and mixing efficiency with latitude and pressure. These changes are most noticeable on the mid-latitude eastern nightside at latitudes near 40° where the flank of the superrotating equatorial jet converges with the nightside high-latitude cyclonic flow. This convergence causes downwelling motion that leads to a negative cloud mixing efficiency in regions where cloud condensate is enhanced and a positive cloud mixing efficiency where cloud condensate is depleted. As a result, the equatorward flank of this region corresponds to negative cloud mixing efficiency and the poleward flank has a positive cloud mixing efficiency at the 100 mbar level. This leads to an enhancement of cloud tracers at higher latitudes and a local depletion in the mid-latitudes. Importantly, this local depletion occurs where the atmosphere is coldest, and the corresponding peak in cloud condensate mass mixing ratio occurs at higher latitudes than the coldest region. As a result, one-dimensional models or three-dimensional dynamical models with equilibrium cloud condensation schemes but without cloud tracers would predict the atmosphere to be cloudy at the cold mid-latitude regions where we find a local minimum in cloud condensate mass mixing ratio. In general, we find that three-dimensional mixing processes set the spatially inhomogeneous cloud condensate and condensable vapor tracer distribution in our GCM simulations.

3.1.4. Three-dimensional Temperature Structure with Varying Cloud Assumptions

The dynamic interaction between the atmospheric circulation, clouds, and radiation sets the three-dimensional

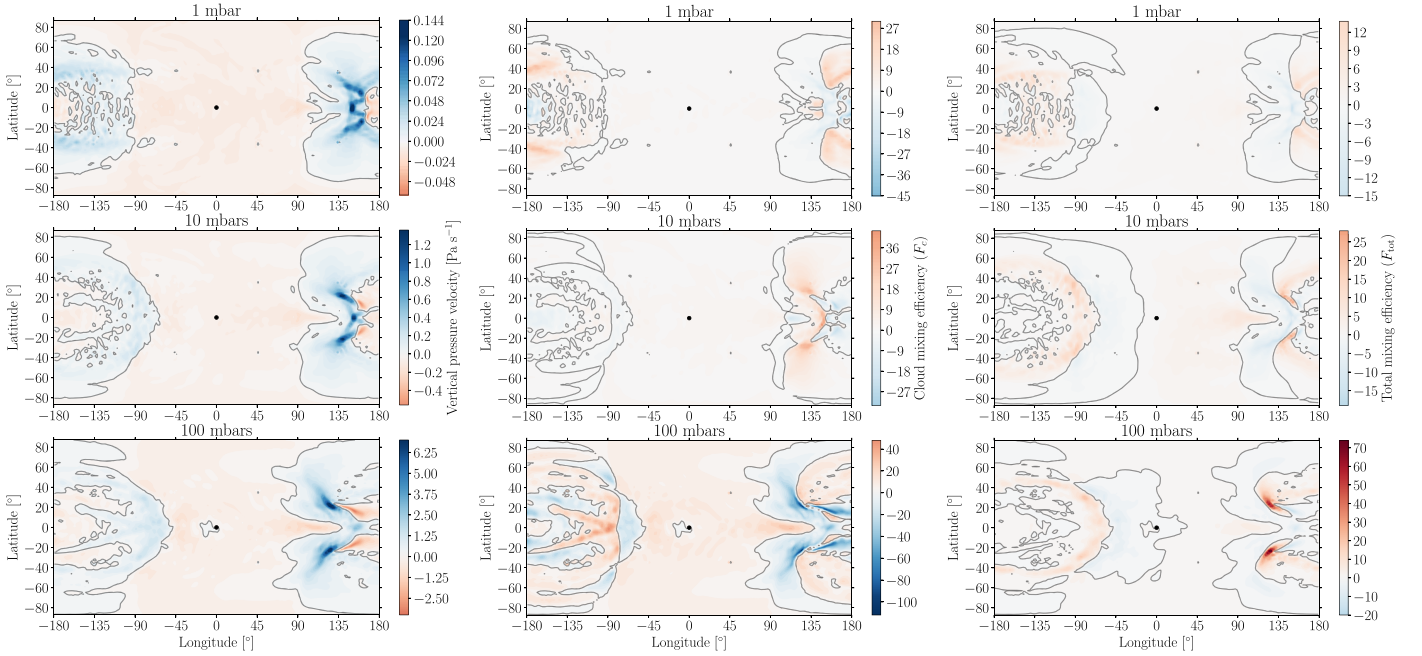


Figure 7. Contour maps of the vertical pressure velocity (left), cloud tracer mixing efficiency (middle), and total (cloud plus vapor) mixing efficiency (right) on the 1, 10, and 100 mbar isobars from the baseline simulation. The solid gray contour denotes the zero vertical velocity or mixing efficiency lines. All panels in each respective column share a color scale. Note that a negative vertical pressure velocity corresponds to upwelling motions and a positive vertical pressure velocity corresponds to downwelling. The mixing efficiency is defined in Equation (26), where $q = q_c$ for the cloud mixing efficiency (middle panels) and $q = q_c + q_v$ for the total mixing efficiency (right-hand panels). Positive mixing efficiency corresponds to local net upward tracer transport, while negative mixing efficiency corresponds to downward net tracer transport. As a result, in both columns red corresponds to upward motion or mixing while blue corresponds to downward motion or mixing. The strong spatial variations in vertical mixing on the nightside promote the patchy nature of nightside cloud coverage.

temperature structure in our GCMs. Figure 8 shows profiles of the meridional mean of temperature as a function of the pressure at the anti-stellar point, west limb, substellar point, and east limb from the cases with varying cloud microphysical and radiative parameters. In all cases, there is a significant change in the temperature profile from day to night, due to the large day–night temperature contrasts at pressures $\lesssim 1$ bar. The eastern limb is everywhere hotter than the western limb due to the eastward advection of warm dayside air by the superrotating equatorial jet. Note that the temperature contrasts between the limbs decrease with decreasing pressure as the flow transitions from an eastward equatorial jet at depth to day–night flow at lower pressures. We also find a thermal inversion at low pressures on the anti-stellar point and west limb in all cases. This thermal inversion causes the conversion of cloud condensate to vapor at low pressures, setting the cloud-top pressure at the anti-stellar point and west limb shown in Figure 6. In Section 4.1, we isolate the thermodynamic impact of hydrogen dissociation and recombination to demonstrate that this thermal inversion is generated by the heat release from recombination of atomic to molecular hydrogen on the nightside and limb.

We find significant differences in the three-dimensional temperature structure between cases with different cloud-radiative assumptions. The deep atmosphere at pressures $\gtrsim 100$ mbar is warmer in the cases with a strong cloud-radiative feedback (the baseline and reduced cloud particle size cases) than in the cases with a weak or zero cloud-radiative feedback (the reduced cloud opacity and no cloud-radiative feedback cases). Figure 9 shows the meridional-mean temperature as a function of the longitude on isobars from 1 bar to 0.1 mbar for the four cases with varying cloud microphysical and radiative parameters. In cases with cloud-radiative feedback, the reduced

outgoing long-wave radiation from the colder cloud tops relative to the deeper underlying atmosphere causes a cloud greenhouse effect that warms the underlying air. This cloud greenhouse effect is strongest on the nightside within the cloud deck (shown in the 100 mbar isobar on Figure 9), and further causes a global increase in the temperature below the cloud deck (see the 1 bar level in Figure 9). Conversely, the cloud greenhouse effect leads to a slight cooling of the nightside atmosphere above the bulk of the cloud deck in cases with strong cloud-radiative feedback, as shown at the 10 and 1 mbar levels in Figure 9. The warming of the deep atmosphere in cases with strong cloud-radiative feedback inhibits cloud condensation at depth, causing the cloud deck to move upward in cases with strong cloud-radiative feedback as shown in Figure 6.

3.2. Emergent Spectra and Phase Curves

We post-process our GCM simulations with the state-of-the-art gCMCART code to predict the effect of cloud microphysical and optical properties on the observable properties of ultra-hot Jupiters. gCMCART is a publicly available⁹ hybrid Monte Carlo radiative transfer (MCRT) and ray-tracing radiative transfer code. The model is described in detail in Lee et al. (2022), and builds upon the MCRT code developed by Hood et al. (2008) to study a range of exoplanet atmospheres (Lee et al. 2017, 2019). gCMCART can natively compute albedo, transmission, and emission spectra at both low and high spectral resolution. Due to its ray-tracing capabilities, gCMCART takes into account the three-dimensional nature of transmission spectra, given that heterogeneities across the limb are expected

⁹ <https://github.com/ELeeAstro>

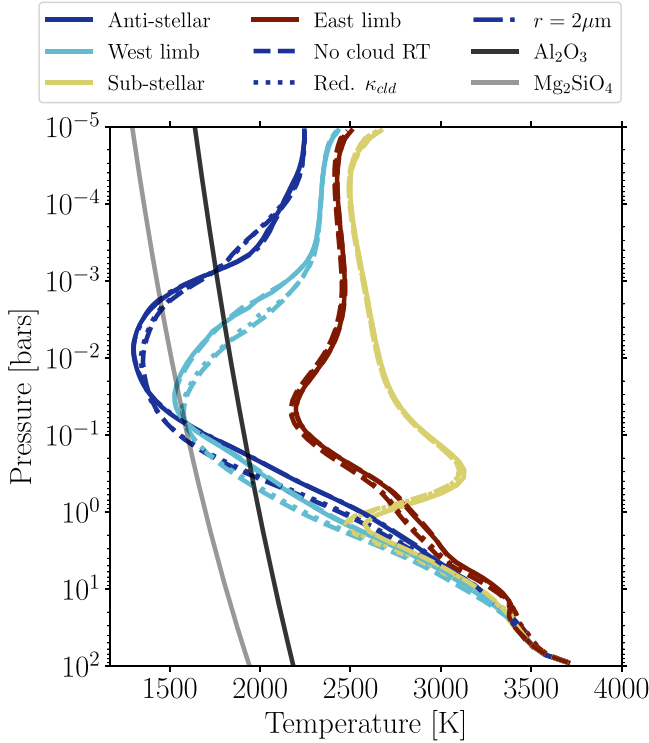


Figure 8. Meridional-mean temperature–pressure profiles from GCM simulations with varying cloud assumptions. Condensation curves for corundum (Wakeford et al. 2017) and forsterite (Visscher et al. 2010) given the solar metallicity are overplotted. We find that varying cloud assumptions impact the three-dimensional temperature structure, and this effect is the largest on the nightside and western limb where corundum cloud condensation can occur. Most notably, cases with significant cloud opacity (baseline and $r = 2 \mu\text{m}$) have hotter nightside atmospheres below the cloud deck than cases with weak or no cloud opacity (No cloud RT, Red. κ_{cld}) due to the cloud greenhouse effect.

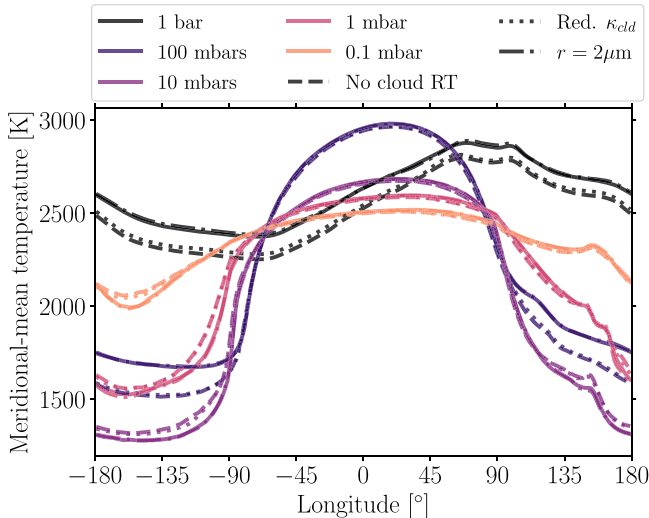


Figure 9. Meridional mean of temperature as a function of the longitude at different pressures from GCM simulations with varying cloud assumptions. We find that the largest differences between cases with large and small or nonexistent cloud opacity occur at pressures $\gtrsim 100$ mbar, due to a cloud greenhouse effect that warms the atmosphere below the nominal cloud deck.

to impact transit observations of ultra-hot Jupiters (Caldas et al. 2019; Pluriel et al. 2020; Wardenier et al. 2022). gCMCRT uses custom k tables, which take cross-section data from both

HELIOS-K (Grimm et al. 2021) and EXOplanet Pressure-broadened LINES (Gharib-Nezhad et al. 2021).

In this work, we apply gCMCRT to compute low-resolution emission spectra, phase curves, and transmission spectra at $R \approx 100$ from our GCM simulations. We use the three-dimensional temperature, atomic hydrogen and condensate cloud tracer mixing ratio, and specific gas constant from the time-averaged end-state of each case. We assume the same cloud particle size distribution as our GCM (see Equation (23)). We discuss the effect of cloud assumptions in the GCM on the phase-dependent emission spectra in Section 3.2.1, predicted phase curves in Section 3.2.2, and resulting transmission spectra in Section 3.2.3.

3.2.1. Phase-dependent Emission Spectra

The planetary emergent spectrum in all of our simulations with cloud tracers is strongly phase-dependent and longitudinally asymmetric due to east–west variations in the partial cloud coverage. Figure 10 shows the planetary emission spectrum as a function of the subobserver longitude from our baseline case and for a subset of subobserver longitudes from cases with varying cloud microphysical and radiative properties. We do not show results from the reduced κ_{cld} case because the behavior of the emergent spectra is similar to the case without cloud-radiative feedback in the GCM. There is a significant east–west asymmetry in the planetary emission spectrum in all cases, with the eastern dayside and limb appearing brighter than the western dayside and limb. This difference is the largest near the peak of the planetary Planck spectrum in the near-infrared. This is expected from previous GCMs of hot Jupiters (e.g., Showman et al. 2009; Heng et al. 2011; Rauscher & Menou 2012; Dobbs-Dixon & Agol 2013; Mayne et al. 2014; Kataria et al. 2016) and occurs because of the strong longitudinal temperature asymmetry driven by the confluence of the planetary-scale wave pattern and super-rotating equatorial jet.

In tandem with the longitudinal asymmetry in flux, there is also a longitudinal asymmetry in the depth of absorption features in the planetary spectrum. In all cases, subobserver longitudes where the planetary disk is centered on the eastern hemisphere have greater absorption feature depths than those centered on the western hemisphere (e.g., compare the 60° and 300° or 120° and 240° lines in the right-hand panel). The lapse rate at the near-infrared photosphere is larger on the western hemisphere (see Figure 8), which would imply stronger absorption features on the cooler western limb due to the larger vertical temperature contrast. However, the cloud deck extends onto the dayside on the western hemisphere, with a global maximum in cloud mass on the nightside near the western limb (see Figure 5). The patchy cloud deck reduces the temperature of the continuum level in emission, resulting in reduced absorption features on the western hemisphere. In general, the combination of temperature structure and cloud coverage acts to shape the emergent spectra in our simulations with cloud tracers.

Though the dayside spectra are similar for our cases with varying cloud assumptions, the nightside emergent spectrum is dependent on both the strength of cloud-radiative feedback and cloud particle size. Figure 11 shows the dayside and nightside emission spectra from our gCMCRT calculations, assuming a PHOENIX stellar spectrum (Allard et al. 2012) appropriate for TOI-1431 ($T_{\text{eff}} = 7690$ K, $\log g = 4.15$, $[\text{Fe}/\text{H}] = 0.43$; Addison

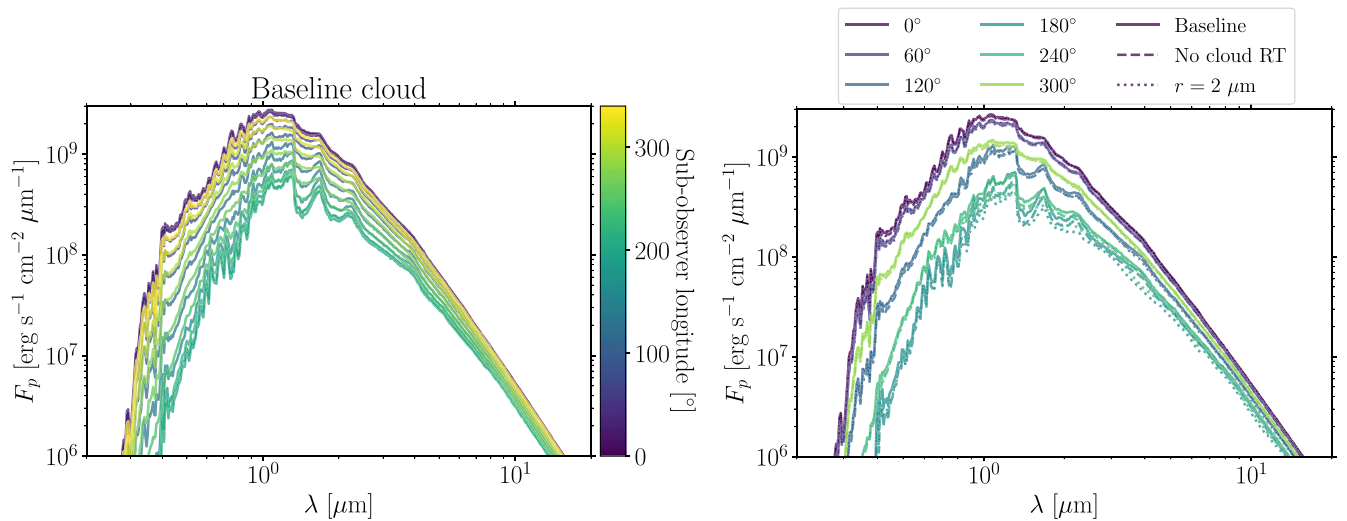


Figure 10. Left: Planetary emergent spectra as a function of the subobserver longitude from the baseline case with active cloud tracers. Right: Comparison of the emergent spectra at six subobserver longitudes between cases with different cloud assumptions. A subobserver longitude of 180° corresponds to transit and 0° corresponds to secondary eclipse. Clouds have the largest impact on the top-of-atmosphere flux on the nightside in the near-infrared.

et al. (2021)), interpolated using the pysnphot package (STScI Development Team 2013). The dayside emission spectra are independent of the inclusion of clouds in the post-processing along with cloud microphysical and radiative assumptions, given that clouds only cover a thin slice of the dayside hemisphere near the western limb.

For nightside emission spectra shown in Figure 11, cloud assumptions cause significant differences in the planet-to-star flux ratio in the near-to-mid-infrared. Notably, the planet-to-star flux ratio on the nightside is larger in the baseline simulation with strongly radiatively active cloud tracers than in those with weak or zero cloud-radiative feedback. Interestingly, this increase in the planet-to-star flux ratio with increasing cloud-radiative feedback is opposite to the effect that cloud-radiative feedback is expected to have on the nightside spectrum of cooler hot Jupiters, where the cold temperature of the cloud top causes the outgoing long-wave radiation on the nightside to decrease (Gao & Powell 2021). As a result, we find a change in the sign of the impact of the nightside cloud greenhouse on the flux emerging from the nightside hemisphere between the regime of hot to that of ultra-hot Jupiters: for hot Jupiters, the cloud greenhouse leads to a decrease in the planetary nightside thermal emission, while in our ultra-hot Jupiter simulations the cloud greenhouse leads to an increase in the outgoing thermal flux from the nightside hemisphere. This change in the behavior of the nightside flux with cloud-radiative feedback occurs because the cloud tracer coverage in our GCMs is patchy rather than uniform, enabling radiation to escape to space from the warmer deep levels in cloud-free regions.

Note that when we do not include clouds in the gCMCRT post-processing, the nightside emitted flux shown in the bottom panel of Figure 11 is larger due to the increased photospheric pressure probing hotter layers. This increase in the nightside planet-to-star flux ratio is especially large in continuum regions with reduced gas opacity. The increase in the nightside flux when removing clouds from the post-processing implies that the change in the sign of the nightside cloud greenhouse effect is not due to clouds pushing the photosphere to lower pressures. Rather, because the cloud deck is sequestered beneath the thermal inversion layer the patchy cloud deck

allows for enhanced emission in relatively cloud-free regions, analogous to the increased thermal emission from Jupiter’s dry $5 \mu\text{m}$ hot spots (Seiff et al. 1998; Showman & Dowling 2000; de Pater et al. 2005).

3.2.2. Phase Curves

The patchy cloud greenhouse effect can potentially impact visible and near-infrared phase curves of ultra-hot Jupiters. Figure 12 shows phase curves including both planetary emission and reflected light due to clouds calculated with gCMCRT in the TESS and Hubble Space Telescope (HST) Wide Field Camera 3 (WFC3) bandpass from GCMs with varying cloud assumptions. All cases show an eastward phase curve offset and large phase curve amplitude, as is typical in GCMs of hot Jupiters (Parmentier & Crossfield 2018). There are only minor differences in the TESS bandpass, with a slight increase in the dayside flux in cases with a stronger cloud greenhouse effect and a slight decrease in the minimum flux in cases with a reduced cloud particle size. Due to the reduced settling velocity of the case with smaller characteristic cloud particle sizes, the greater cloud mass at low pressures reduces the nightside cloud-top temperature in the case with a reduced particle size (see Figure 20).

Note that none of the GCMs in our model grid can match the observed TESS phase curve of TOI-1431b, as the observations of Addison et al. (2021) found a nightside planet-to-star flux ratio of 49^{+5}_{-4} ppm while our baseline simulation predicts a nightside planet-to-star flux ratio of just 10.7 ppm. This may suggest that another process besides the cloud greenhouse effect and hydrogen dissociation and recombination are required to explain the hot nightside temperature of TOI-1431b (and the similar HAT-P-7b; Bell et al. 2021). However, we caution that our GCMs are idealized in order to provide a framework to understand the processes that set the cloud distributions of ultra-hot Jupiters, and as a result more sophisticated nongray GCMs may better match the observed phase curve (see Section 4.3). Additionally, spectrophotometric observations at longer wavelengths can provide additional context for the TESS phase curve observation of TOI-1431b. Notably, the predicted phase curves from our GCMs in the

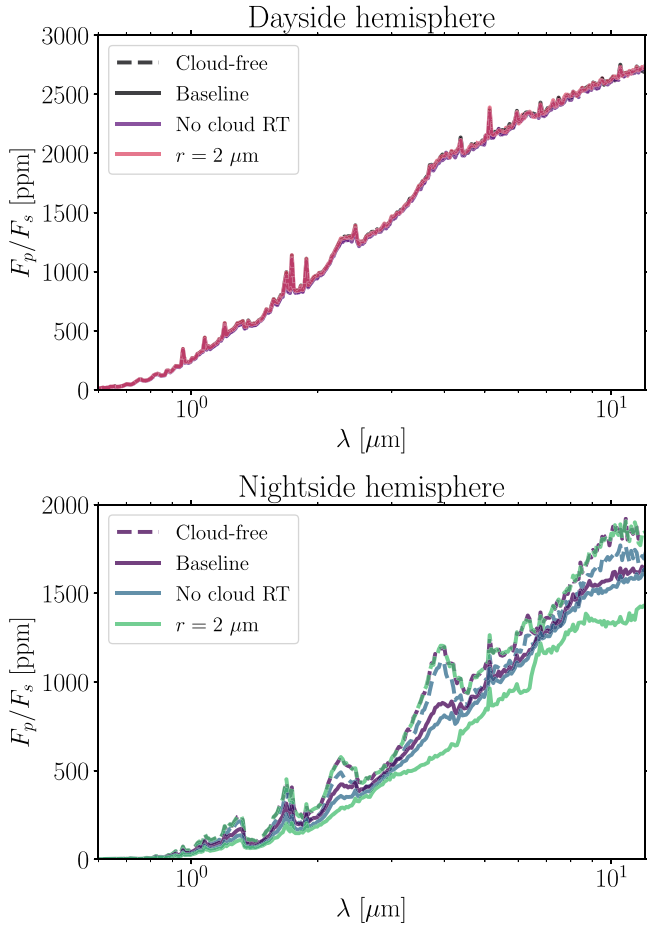


Figure 11. Simulated emission spectra for the dayside hemisphere (i.e., at secondary eclipse, top) and the nightside hemisphere (i.e., at transit, bottom) for cases with different cloud assumptions. Predictions that do not include clouds in the gCMCRT post-processing are shown with dashed lines, while cases that include clouds in both the GCM and post-processing are shown by solid lines. The dayside emission spectrum is unaffected by cloud assumptions, given the small amount of clouds on the dayside in our GCM simulations. The nightside emission spectrum is strongly affected by the inclusion of clouds, and in cases with clouds it is both affected by including significant cloud-radiative feedback in the GCM and varying the cloud particle size. The cases that do not include clouds in the post-processing have a higher emitted nightside flux than cloudy cases as emission from hotter regions at depth can more readily escape to space. The baseline case with radiatively active clouds has a higher nightside flux in the near- and mid-infrared than the reduced cloud opacity and no cloud-radiative feedback cases. This is due to the patchy nightside cloud greenhouse effect warming the atmosphere below the cloud deck, which in turn increases the planetary long-wave radiation that escapes to space in less cloudy regions near the anti-stellar point.

WFC3 bandpass show larger differences than in the TESS bandpass on the nightside hemisphere of up to tens of ppm between the cases with strong and weak cloud-radiative feedback. As for the nightside emergent flux shown above, this is due to the effect of the patchy cloud greenhouse warming the deep atmosphere and increasing the flux that escapes to space from the nightside hemisphere centered on the anti-stellar point.

3.2.3. Transmission Spectra

We find that condensate clouds likely do not have a significant impact on the transmission spectra of ultra-hot Jupiters with equilibrium temperatures comparable to or greater than TOI-1431b ($T_{\text{eq}} \gtrsim 2370$ K). The top panel of Figure 13

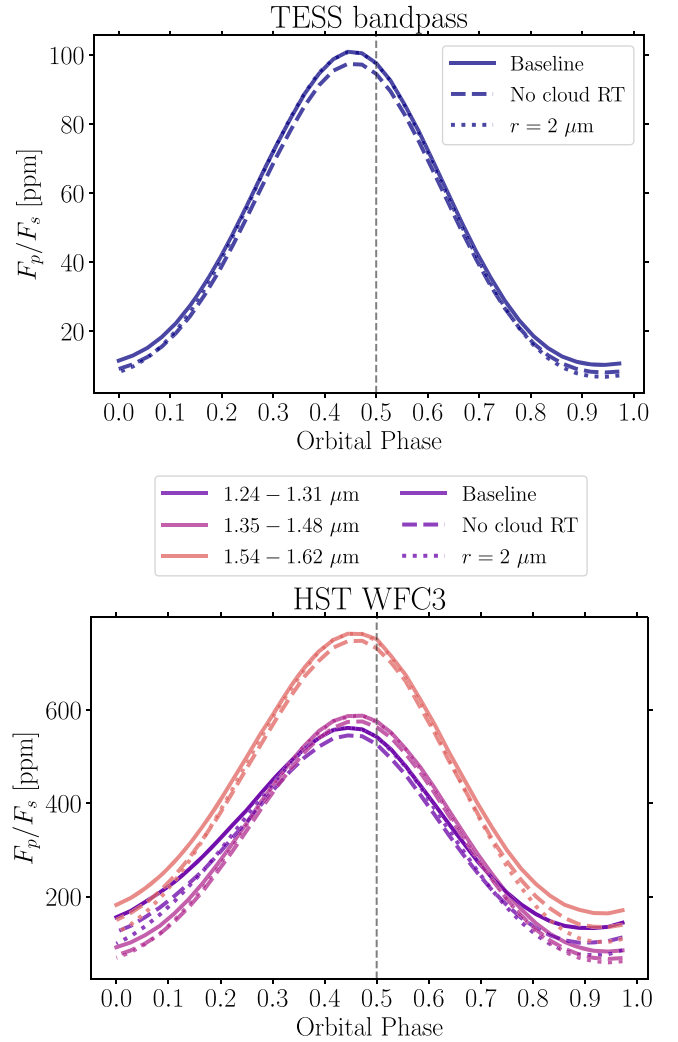


Figure 12. Simulated phase curves for varying cloud assumptions. The top panel shows the phase curves in the TESS bandpass, while the bottom panel shows phase curves at three different wavelength bands within the HST WFC3 bandpass. Secondary eclipse at an orbital phase of 0.5 is shown by the vertical dashed line. We find that the inclusion of significant cloud-radiative feedback in the GCM increases the peak flux, and that cases with a smaller characteristic cloud particle size have a reduced minimum level of nightside flux.

shows predicted transmission spectra from the baseline case both including and removing the scattering and absorption by clouds. We find that the inclusion of clouds slightly raises the continuum level of absorption, especially blueward of the $1.4 \mu\text{m}$ water absorption feature accessible with HST/WFC3. However, even the high-temperature condensate corundum clouds considered here do not have a significant impact on the amplitudes of spectral features in transmission. The bottom panel of Figure 13 shows the impact of cloud microphysical and radiative properties on our simulated transmission spectra. The transit depth in the near and mid-infrared is somewhat larger in cases with a significant cloud-radiative feedback than those with a weak cloud-radiative feedback. This is because the thermal impact of the cloud greenhouse shifts the cloud deck to lower pressures in cases with a strong cloud-radiative feedback, enhancing the scattering and absorption of transmitted stellar light at high altitudes.

In the cases with a significant cloud-radiative feedback, condensate cloud tracers in the GCM are lofted to low pressures of a few mbar on the western limb (see Figure 6).

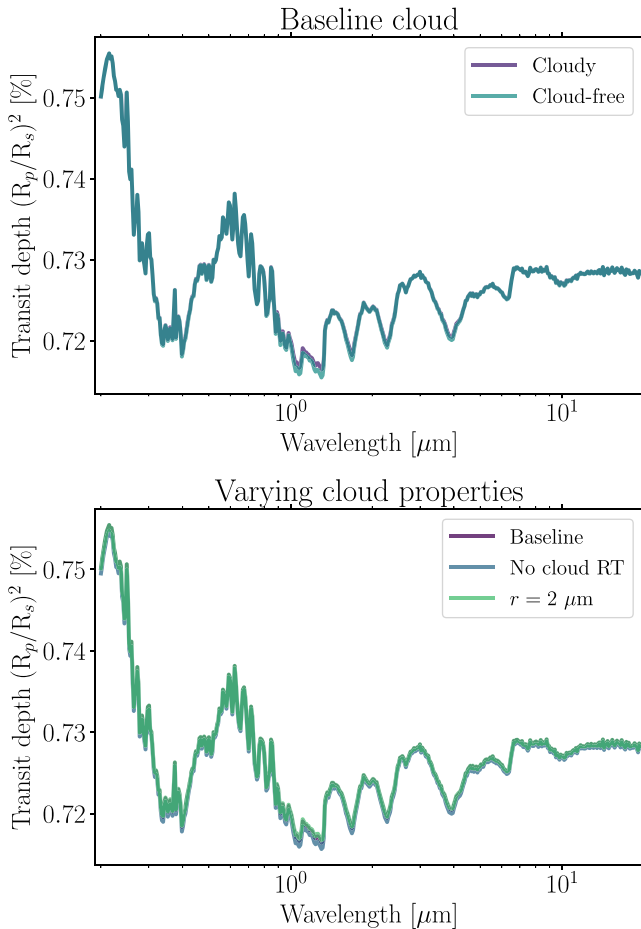


Figure 13. Simulated transmission spectra for varying cloud assumptions. The top panel shows simulated transmission spectra from our post-processed baseline GCM with active clouds, both including and ignoring the effect of clouds in the post-processing. The bottom panel shows simulated transmission spectra including the impact of clouds from our suite of models with varying cloud properties. We find that clouds do not have a significant impact on the continuum level of transmission spectra of ultra-hot Jupiters. The effect of clouds on transmission spectra is the largest in cases with significant cloud-radiative feedback due to their higher altitude cloud decks.

This cloud-top pressure is similar to that expected from GCMs of WASP-121b that were post-processed to include clouds (Parmentier et al. 2018; see their Figure 11), however here we include the dynamic transport of and radiative feedback due to clouds in the GCM itself. Our finding that the western limb is cloudy to low pressures and the eastern limb is cloud-free further implies strong limb-to-limb contrasts in the cloud coverage of ultra-hot Jupiters, as expected from previous microphysical modeling (Powell et al. 2019; Helling et al. 2021). However, as found in the case of WASP-178b (Lothringer et al. 2022), we predict that SiO vapor can persist in the gas phase and produce strong transmission spectral features in the NUV.

4. Discussion

4.1. Effect of An Enhanced Visible Opacity and Hydrogen Dissociation and Recombination On Thermal Structure

We included a case with a significantly enhanced visible opacity in our suite of models in order to mimic the potential radiative impact of absorption of incident starlight by atomic metals in the atmospheres of ultra-hot Jupiters (Lothringer et al.

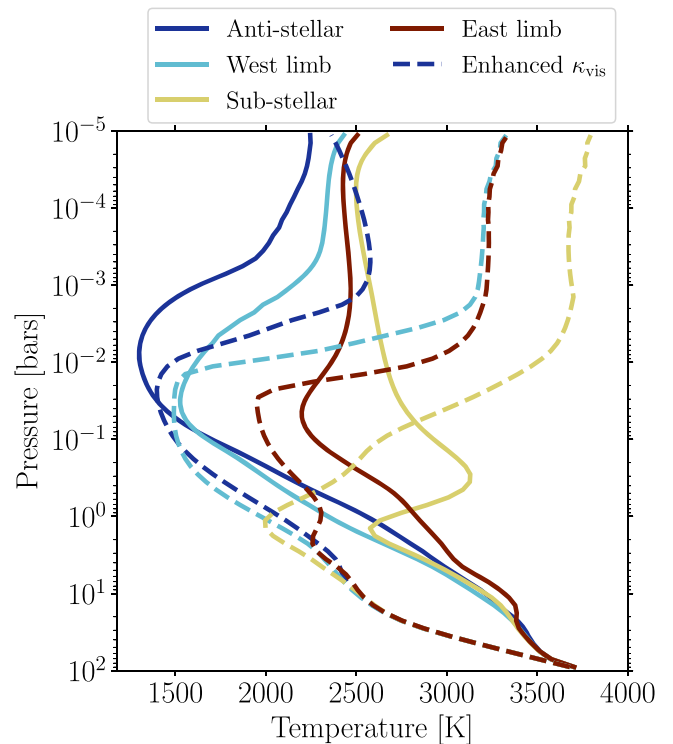


Figure 14. Impact of enhanced visible opacity on the simulated thermal structure. Shown are meridional-mean temperature profiles from the baseline cloud case (solid lines) and a case with enhanced visible opacity (dashed lines). A large ($\gtrsim 1500$ K) thermal inversion on the dayside in the enhanced visible opacity case leads to a dynamically induced ~ 1000 K thermal inversion on the nightside that occurs at higher pressures than in the baseline case. This deeper and stronger nightside thermal inversion in the enhanced visible opacity run prevents significant cloud formation on the nightside.

2018). Another rationale for studying the impact of enhanced visible opacity is to determine the effect of a dayside inversion on the global dynamics and resulting three-dimensional temperature structure. In the double-gray or band-gray framework, an enhanced visible wavelength opacity warms the dayside upper atmosphere, causing deeper layers to cool to maintain global radiative equilibrium (Guillot 2010; Parmentier & Guillot 2014; Parmentier et al. 2015). Additionally, with a thermal inversion the hotter upper layers on the dayside have a shorter radiative cooling timescale, which would naively imply reduced day-to-night heat transport at low pressures (Perez-Becker & Showman 2013; Komacek & Showman 2016; Zhang & Showman 2017). However, a thermal inversion also causes an increased abundance of hydrogen in atomic form at low pressures due to thermal dissociation (see Figure 19). As this atomic hydrogen is transported from dayside to nightside, it will recombine and warm the surrounding atmosphere (Bell & Cowan 2018; Tan & Komacek 2019), affecting the global temperature structure.

Figure 14 compares meridional-mean temperature–pressure profiles at the anti-stellar point, west limb, substellar point, and east limb between the baseline case and the case with an enhanced visible opacity. The case with an enhanced visible opacity has a strong dayside thermal inversion, while the baseline case is noninverted on the dayside at pressures $\lesssim 300$ mbar. However, *both* cases have a significant thermal inversion on the nightside and western limb. This nightside inversion has a larger amplitude in the case with an enhanced visible opacity, but begins at a pressure of ~ 10 mbar

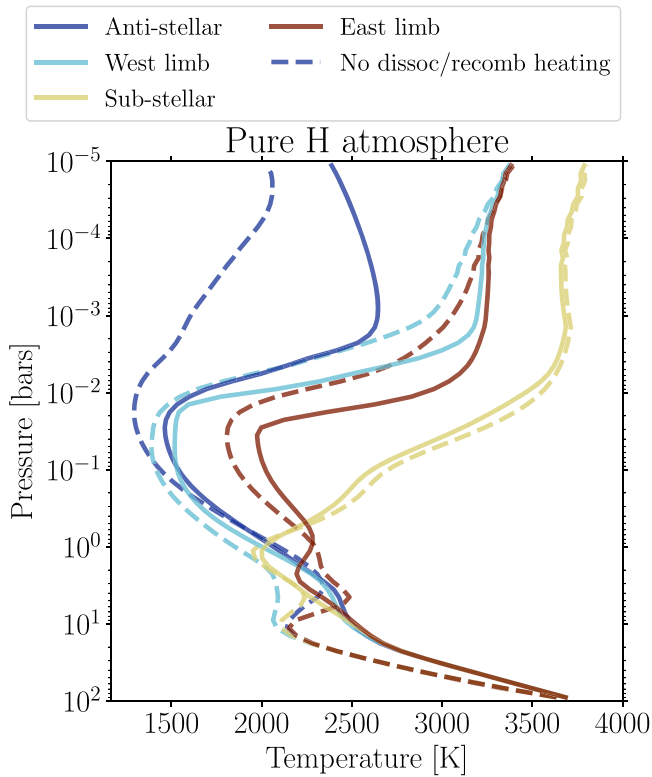


Figure 15. Impact of hydrogen dissociation and recombination on the thermal structure of ultra-hot Jupiters. Shown are profiles of the meridional-mean temperature from cases with an enhanced visible opacity and a pure hydrogen atmosphere with and without the heating/cooling from hydrogen recombination/dissociation, resulting in a maximal effect of hydrogen recombination on the thermal structure. The removal of the thermal effect of hydrogen dissociation and recombination reduces the strength of the nightside thermal inversion.

in both cases. As a result, the deepest levels at which there is a nightside inversion coincide with pressures where the atmospheric flow is characterized by a strong eastward equatorial jet. Additionally, as shown below, the nightside inversion is significantly weakened with the removal of the thermodynamic impact of hydrogen dissociation and recombination. As a result, we hypothesize that on planets with strong (~ 1000 K) dayside thermal inversions, nightside thermal inversions can be sustained at low pressures (at much lower pressure levels than the cloud-free thermal photosphere; see Table 1) due to the effective additional day–night heat transport from the conversion of atomic to molecular hydrogen.

To isolate the effect of hydrogen dissociation and recombination on the atmospheric circulation and temperature structure, we conducted additional GCMs with the thermodynamic heating and cooling term from hydrogen dissociation and combination in Equation (5) set to zero. These models retain the same atomic hydrogen tracer formalism as the other GCMs conducted, and as a result retain the effect of hydrogen dissociation and recombination on the mean molecular weight, specific gas constant, and heat capacity. We conducted two additional simulations: a case maximizing the impact of hydrogen dissociation and recombination by considering an atmosphere comprised entirely of hydrogen (i.e., no helium, with $x_{\text{He}/\text{H}} = 0$), with the same visible-band and infrared-band opacity choices as in our “enhanced visible opacity” simulation, and without radiatively active cloud tracers; and an

equivalent case to that just described but without the thermal effect of hydrogen dissociation and recombination.

Figure 15 compares the temperature structure between the case with a maximal impact of hydrogen dissociation and recombination on the thermal structure and an equivalent case without the thermal effect of hydrogen dissociation and recombination. Due to the high visible opacity in this case, the dayside has a strong and deep thermal inversion similar to that in the equivalent case in our full model suite with enhanced visible opacity. The dayside thermal inversion is slightly stronger in the simulation without the thermal effect of hydrogen dissociation leading to cooling on the dayside. The heating due to hydrogen recombination causes the temperature on the limb at pressures of $100 \mu\text{bar} \lesssim p \lesssim 1$ bar to be higher in the case with the thermal effect of hydrogen dissociation and recombination, although both cases have thermal inversions on each limb. Further, the temperature increase due to the nightside inversion is much larger in the case with the thermal effect of hydrogen dissociation and recombination¹⁰, leading to nightside temperatures that can be over 1000 K warmer than in the case without heating due to hydrogen recombination.

The strong change in the three-dimensional thermal structure at low pressures due to the thermodynamic effects of hydrogen dissociation and recombination may have implications for phase-resolved observations of ultra-hot Jupiters. Notably, such a nightside inversion has not been found in recent low-resolution phase curves of the ultra-hot Jupiters WASP-76b and WASP-121b, which both show evidence for a dayside thermal inversion but a noninverted nightside temperature profile (May et al. 2021; Mikal-Evans et al. 2022). However, because the photosphere of tidally locked gas giants is horizontally nonuniform (Dobbs-Dixon & Cowan 2017), these low-resolution observations probe higher pressure levels on the nightside than on the dayside. The HST phase curve of WASP-121b probes pressures of ~ 10 – 100 mbar on the nightside, deeper than the nightside temperature inversion that occurs in our GCMs due to the thermal impact of hydrogen recombination that lies at pressures of 1–10 mbar. However, as discussed in Section 4.3, we caution that our GCM is double-gray and may not adequately model radiative cooling from recombined molecules on the nightside. Further observational constraints on the presence of dayside and nightside inversions from both low-resolution phase curves and high-resolution phase-dependent emission spectra would help determine how the interplay between atmospheric dynamics and molecular dissociation and recombination affect the thermal structure of ultra-hot Jupiters.

4.2. The Impact of Patchy Clouds On Emergent Properties of Ultra-hot Jupiters

Our GCMs with radiatively active cloud tracers support the findings of previous cloud microphysical and GCM models that predict a transition in cloud coverage between hot and ultra-hot Jupiters, with hot Jupiters having uniformly cloudy nightsides and ultra-hot Jupiters having nonuniform cloud distributions (Gao & Powell 2021; Helling et al. 2021; Parmentier et al.

¹⁰ Note that there is still a slight thermal inversion at low pressures at the anti-stellar longitude in the case without the thermal effect of hydrogen dissociation. This occurs because the day-to-night winds increase in speed with decreasing pressure, while the radiative timescale is relatively independent of pressure in the upper regions of double-gray models. Given that the substellar longitude is nearly isothermal at pressures $\lesssim 1$ mbar, this leads to a relative increase in the substellar-to-anti-stellar heat transport with decreasing pressure in the upper regions of the model.

2021; Roman et al. 2021). We find that the patchy cloud coverage on ultra-hot Jupiters causes their nightside cloud greenhouse to have a different effect on observable properties than cooler hot Jupiters. For hot Jupiters, the uniform nightside cloud deck constrains the source of outgoing long-wave radiation to the region near the cloud top, reducing the outgoing flux compared to a cloud-free nightside (Gao & Powell 2021). In contrast, the patchy nightside clouds of ultra-hot Jupiters can locally enhance the thermal flux that escapes to space. This occurs because, as with a uniform cloud deck, the cloud greenhouse effect warms the deep atmosphere. However, unlike a uniform cloud deck, the patchiness of nightside clouds on ultra-hot Jupiters enables thermal emission from the warmer levels at depth to escape to space in regions with reduced cloud opacity. As a result, we find a change in the sign of the cloud greenhouse effect on the outgoing thermal flux from the nightside hemisphere of ultra-hot Jupiters as compared to hot Jupiters. This suggests that the radiative feedback due to the patchy cloud deck plays a role in the break of the flat nightside temperature trend between the hot and ultra-hot Jupiters inferred from the sample of Spitzer phase curves (Beatty et al. 2019; Keating et al. 2019; Bell et al. 2021).

Additionally, the patchy cloud greenhouse effect in our GCM simulations implies that there will be a trade-off between the patchy cloud coverage and cloud greenhouse effect that controls how the nightside temperature depends on equilibrium temperature. This is because in isolation, cloud dissipation at hotter equilibrium temperatures (i.e., higher incident stellar flux) leads to an increase in the nightside flux as the hot deep levels can more easily radiate to space. However, at the same time the reduction in the cloud coverage leads to slightly cooler temperatures at depth due to the reduced cloud greenhouse effect. The competition between patchy cloud coverage and the cloud greenhouse effect itself depends on the three-dimensional cloud distribution, necessitating a suite of three-dimensional models of ultra-hot Jupiters with radiatively active cloud tracers covering a broad range of equilibrium temperature in order to determine the resulting dependence of outgoing long-wave radiation on planetary irradiation.

We find that in our simulations with radiatively active cloud tracers, high-temperature condensate clouds can be mixed to low (~ 5 mbar) pressures, but only have a slight effect on transmission spectra. This agrees with the expectation from both GCMs with post-processed clouds (Parmentier et al. 2018) and cloud microphysics models (Helling et al. 2021) that condensate clouds can persist at \sim mbar pressures; however we do not find that clouds have a significant impact on transmission spectra of ultra-hot Jupiters with equilibrium temperatures comparable to or greater than TOI-1431b. Additionally, we find that strong limb-to-limb asymmetries in cloud coverage due to the large temperature contrast between the eastern and western limb (Powell et al. 2019) extend into the ultra-hot Jupiter regime, as potentially implied by recent time-resolved high-resolution transmission spectra of WASP-76b (Ehrenreich et al. 2020; Kesseli & Snellen 2021).

We expect that the transition point between cloudy and cloud-free limbs as probed in transmission will occur within the ultra-hot Jupiter regime. From an emerging sample of NUV spectra of ultra-hot Jupiters, there is tentative evidence that such a transition occurs between equilibrium temperatures of 1950–2450 K (Lothringer et al. 2022). For WASP-121b ($T_{\text{eq}} \approx 2350$ K), Mikal-Evans et al. (2022) found sufficiently

cold nightside temperatures from HST/WFC3 phase curve observations for cloud condensation, while previous transmission spectra of WASP-121b point toward a cloud-free limb—implying that atmospheric motions keep condensate clouds aloft in order to prevent rain-out to deeper atmospheric levels. Our GCM simulations with an equilibrium temperature of 2368 K show nightside cloud coverage that extends only slightly past the western limb, which lies at a similar planetary irradiation to the tentative observational transition in limb cloud coverage. However, a variety of planetary properties along with equilibrium temperature, including gravity and atmospheric metallicity, conspire to affect cloud microphysics and horizontal and vertical transport. This motivates observational surveys of both NUV and high-resolution transmission spectra as well as thermal phase curves to probe the transition in global climate and condensate cloud coverage between the hot and ultra-hot Jupiters. In addition, time-resolved high-resolution transmission and emission spectroscopy will be a powerful tool to test the expected patchy cloud configuration for individual ultra-hot Jupiters.

4.3. Limitations

Our current modeling framework is simplified in order to lend physical understanding of how a coupling between atmospheric dynamics and cloud-radiative feedback sets the cloud coverage in ultra-hot Jupiter atmospheres. Due to its idealized nature, our model setup has a variety of limitations that must be addressed before detailed comparison with observations of ultra-hot Jupiters. Most notably, as in many recent GCM studies of exoplanet atmospheric dynamics and its impact on observations (e.g., Dietrick et al. 2020; May & Rauscher 2020; Mendonca 2020; Beltz et al. 2021; Roman et al. 2021; Harada et al. 2021; May et al. 2021; Beltz et al. 2022), our model utilizes a double-gray radiative transfer scheme. Though double-gray schemes provide a simplified yet realistic framework within a GCM to gain physical insight into the processes that regulate atmospheric dynamics and heat transport, Lee et al. (2021) recently demonstrated that GCMs with double-gray radiative transfer provide an inadequate representation of the thermal structure compared to those with band-gray or fully nongray radiative transfer schemes. As a result, we caution that the quantitative predictions for thermal structure and cloud coverage may differ between our idealized GCMs and models with more realistic radiative transfer schemes.

Importantly, nongray models are required to fully understand the provenance of nightside inversions in ultra-hot Jupiters. Notably, the upper layers of the nightside will be cold enough for at least partial recombination of molecules (e.g., H_2O). Low pressures on the nightside will then undergo enhanced infrared cooling to space from molecular lines that may offset the thermodynamic warming impact of hydrogen recombination. Results from our idealized models, including patchy nightside clouds and a dynamically induced nightside thermal inversion, motivate future work with nongray radiative transfer to fully determine how the thermal impact of hydrogen dissociation and recombination affects the temperature structure of ultra-hot Jupiters at low pressures.

In this work, we have isolated the cloud-radiative feedback from a single high-temperature condensate, corundum, in order to study how the localized nature of vertical mixing and cloud-radiative feedback sets the patchy cloud coverage on the

nightsides of ultra-hot Jupiters. Though our simulated ultra-hot Jupiter has an equilibrium temperature above the condensation temperature of even high-temperature condensates at pressures $\lesssim 1$ bar, the simulated temperatures on the nightside in our GCM suite can be cold enough that a large variety of cloud species could locally condense, including silicates, sulfates, iron, and high-temperature condensates (e.g., perovskite). Additionally, microphysical models of cloud formation across the hot to ultra-hot Jupiter transition predict that a range of cloud condensate species can locally form on the nightside and western limb of ultra-hot Jupiters (Gao & Powell 2021; Helling et al. 2021). Notably, the high optical thickness of silicate clouds (especially forsterite) may regulate the cooling from a patchy nightside cloud deck. Future work including multiple types of condensate cloud tracers is required to ascertain how the formation, dynamical mixing, and radiative feedback of the range of possible cloud condensates affect the atmospheric dynamics and observable properties of ultra-hot Jupiters.

Though the cloud particle size distribution and cloud-radiative parameters (e.g., asymmetry parameter, single scattering albedo) used for the GCM simulations conducted in this work are informed by CARMA cloud microphysics simulations (Gao et al. 2020; Gao & Powell 2021), they neglect the dynamic three-dimensional interaction between the atmospheric dynamics and cloud microphysics. In reality, the cloud particle size distribution will evolve significantly due to the competition between cloud nucleation, vertical mixing, and settling, which will in turn affect the cloud optical thickness and the radiative scattering and absorption due to the cloud deck. The radiative feedback of clouds will then affect the dynamics, resulting in a coupled interplay between cloud microphysics, atmospheric circulation, and radiative transfer. Though we have included the interplay between the latter two in this work, we expect that a self-consistent inclusion of cloud microphysical processes would impact the resulting patchy cloud distribution. Previous GCMs with self-consistently coupled cloud microphysics (e.g., Lee et al. 2016; Lines et al. 2018) have found, albeit at great computational expense, that this coupling has a significant impact on the atmospheric dynamics and emergent properties of hot Jupiters.

Lastly, we only considered a single planetary parameter regime in this work in order to isolate the impact of cloud microphysical and radiative assumptions on the atmospheric circulation and cloud coverage of ultra-hot Jupiters. Future work is required to understand the coupled impact of cloud mixing and radiative feedback on the cloud coverage of hot gas giants across the transition from hot Jupiters to ultra-hot Jupiters. This broad parameter sweep would be necessary to test the prediction from one-dimensional models that the dissipation of the forsterite cloud deck leads to the increased nightside brightness temperatures of ultra-hot Jupiters (Gao & Powell 2021), as well as to further study how the coupling between mixing and radiative feedback of clouds impacts the phase curves of hot and ultra-hot Jupiters (Parmentier et al. 2021; Roman et al. 2021).

5. Conclusions

Ultra-hot Jupiters have been found to be a unique class of exoplanet because of observational evidence for molecular dissociation, atomic ionization, and heavy metal vapor on their daysides. In this work, we have demonstrated using three-

dimensional general circulation models with radiatively active high-temperature condensate cloud tracers that ultra-hot Jupiters are also unique because their cloud coverage is inherently patchy, as cloud condensation and vertical transport of condensed aerosol is only possible on the nightside and western limb of the planet. This is in broad agreement with previous theoretical work that has predicted a transition in cloud coverage between hot and ultra-hot Jupiters (Powell et al. 2019; Gao et al. 2020; Helling et al. 2021; Parmentier et al. 2021; Roman et al. 2021). This also agrees with observational work that has found evidence for the clearing of a uniform nightside cloud deck at the transition between hot and ultra-hot Jupiters by studying the dependence of nightside outgoing long-wave radiation with incident stellar irradiation (Beatty et al. 2019; Keating et al. 2019). Below we outline our key conclusions from this work, along with future avenues for further exploration of cloud-radiative feedback on the dynamics of ultra-hot substellar atmospheres.

1. The majority of ultra-hot Jupiters detected to date represent a transitional state in cloud coverage between hot Jupiters and cloud-free substellar objects (e.g., KELT-9b). While hot Jupiters are expected to have a nearly uniform blanket of nightside cloud coverage that acts to absorb and re-emit thermal radiation at nearly uniform cool cloud-top temperatures, there are only certain regions where cloud condensation is favorable on the nightsides of ultra-hot Jupiters—even for the highest-temperature condensates. This causes the nightside and limb cloud distributions of ultra-hot Jupiters to be patchy and dependent on the nature of the atmospheric circulation and temperature structure.
2. We find that the patchy spatial distribution of clouds in ultra-hot Jupiter atmospheres does not directly track the local temperature conditions in the atmosphere. Notably, we find a lack of clouds in the coldest mid-latitude regions of the planet in every simulation in our suite of GCMs with varying cloud microphysical and radiative properties. This is because net vertical mixing of aerosols in a stably stratified atmosphere requires a positive correlation between tracer abundance and upward vertical winds (Parmentier et al. 2013; Zhang & Showman 2018a, 2018b). In these mid-latitude regions, downwelling due to convergence at the flanks of the superrotating equatorial jet leads to net downward transport of cloud condensate, further enhancing the already patchy nature of the cloud deck on a given isobar.
3. We find in all of our GCMs with radiatively active or inactive cloud tracers that the patchy nightside cloud decks of ultra-hot Jupiters are sequestered at depth. The cloud deck does not reach pressures significantly below 1 mbar at any location for any model in our suite of GCMs. This deep sequestration of condensate clouds is due to a dynamically induced thermal inversion on the nightside that is caused by the local heat deposition by hydrogen recombination, as a significant fraction of the atomic hydrogen transported from the dayside at low pressures recombines into molecular hydrogen.
4. The combination of spatially patchy cloud coverage and sequestration of clouds at depth in our simulations causes high-temperature condensate clouds to have a greenhouse effect on the atmosphere below. Post-processing of our GCMs with the state-of-the-art Monte Carlo radiative

transfer code `gCMCRT` shows that this patchy cloud greenhouse can have a potentially significant effect on the nightside emission spectra of ultra-hot Jupiters. Notably, this cloud greenhouse effect causes an increase in the emergent flux from the nightside hemisphere of ultra-hot Jupiters, in contrast to the expected decrease in the outgoing long-wave radiation due to the cloud greenhouse inferred for cooler hot Jupiters (Gao & Powell 2021). This is because the patchy nature of the cloud deck enables radiation to escape to space from relatively clear regions warmed by the cloud greenhouse. Additionally, we predict that the deep patchy cloud condensate coverage on the limbs of ultra-hot Jupiters with equilibrium temperatures of $\gtrsim 2370$ K does not greatly impact transmission spectra from the NUV to mid-infrared.

5. In this work, we have only modeled the coupled dynamical transport of and radiative feedback by a single cloud condensate, corundum. We did so in order to cleanly investigate the transport of high-temperature condensates in ultra-hot Jupiter atmospheres that persist up to the irradiation level where ultra-hot Jupiter atmospheres become cloud-free. Future work is required to study the coupled impact of corundum along with other potentially abundant cloud species, especially silicates, along with other high-temperature cloud condensates (e.g., perovskite). Further work could investigate how the combined radiative and dynamical coupling of a combination of cloud condensates in GCMs impacts predictions for the transition in nightside and limb cloud coverage from hot to ultra-hot Jupiters along with the impact of these dynamically and radiatively active clouds on observable properties of the range of tidally locked gas giant atmospheres.

A significant portion of this work was performed on land that is the traditional homeland of the Piscataway and Nacotchtank peoples. We thank the anonymous referee for an insightful report that improved this work. X.T. is supported by the European Research Council advanced grant EXOCONDENSE (PI: R.T. Pierrehumbert). This work was completed with resources provided by the University of Chicago Research Computing Center (PI: Jacob Bean). The authors acknowledge the University of Maryland supercomputing resources (<http://hpcc.umd.edu>) made available for conducting the research reported in this paper.

Appendix A

Effect of Cloud-radiative Assumptions On Atmospheric Dynamics and Cloud Distribution

A.1. Temperature, Winds, and Atomic Hydrogen Mass Mixing Ratio

Equivalent maps to those for the baseline case in Figure 2 displaying the temperature and wind patterns as well as the hydrogen mass mixing ratio and regions with significant cloud mass mixing ratio on isobars are shown for the remaining cases from the full suite of GCMs in Figures 16–19. The largest differences between the baseline case and the cases with weak cloud-radiative feedback (i.e., the case no cloud-radiative feedback shown in Figure 16 and the case with a weakened cloud-radiative feedback in Figure 17) is the cooler deep atmosphere in the cases with a weak or nonexistent cloud-radiative feedback due to the lack of a cloud greenhouse effect. This causes the cloud deck to move to higher pressures, allowing cloud condensate to persist on the mid-latitude nightside to pressures of a bar. There are only minor differences in the temperature and cloud mixing ratio pattern between the baseline case and the case with a reduced cloud particle size shown in Figure 18. This is because the cloud particle size affects just the vertical settling of clouds in our numerical scheme, while the cloud-radiative feedback and temperature structure has a larger control on the resulting cloud distribution. Regardless, the deep atmosphere is slightly warmer in the case with a reduced particle size than in the baseline case due to the thicker cloud deck caused by the reduced settling velocity with smaller characteristic cloud particle sizes.

Figure 19 shows the temperature and wind as well as the atomic hydrogen mass mixing ratio on isobars from the case with an enhanced visible opacity. The enhanced absorption of incoming stellar radiation leads to significant differences in temperature and winds relative to the other four cases in our model suite. The model with an enhanced visible opacity has a global thermal inversion at low pressures (see also Section 4.1), with a larger-amplitude thermal inversion on the dayside than nightside leading to significant day-to-night temperature contrasts at all pressures. This thermal inversion causes almost the entire dayside to have its hydrogen in atomic state at pressures $\lesssim 1$ mbar. The thermal inversion also prevents significant cloud formation, as no clouds form with a mixing ratio $\geq 10^{-6}$ kg kg⁻¹ in the case with an enhanced visible opacity.

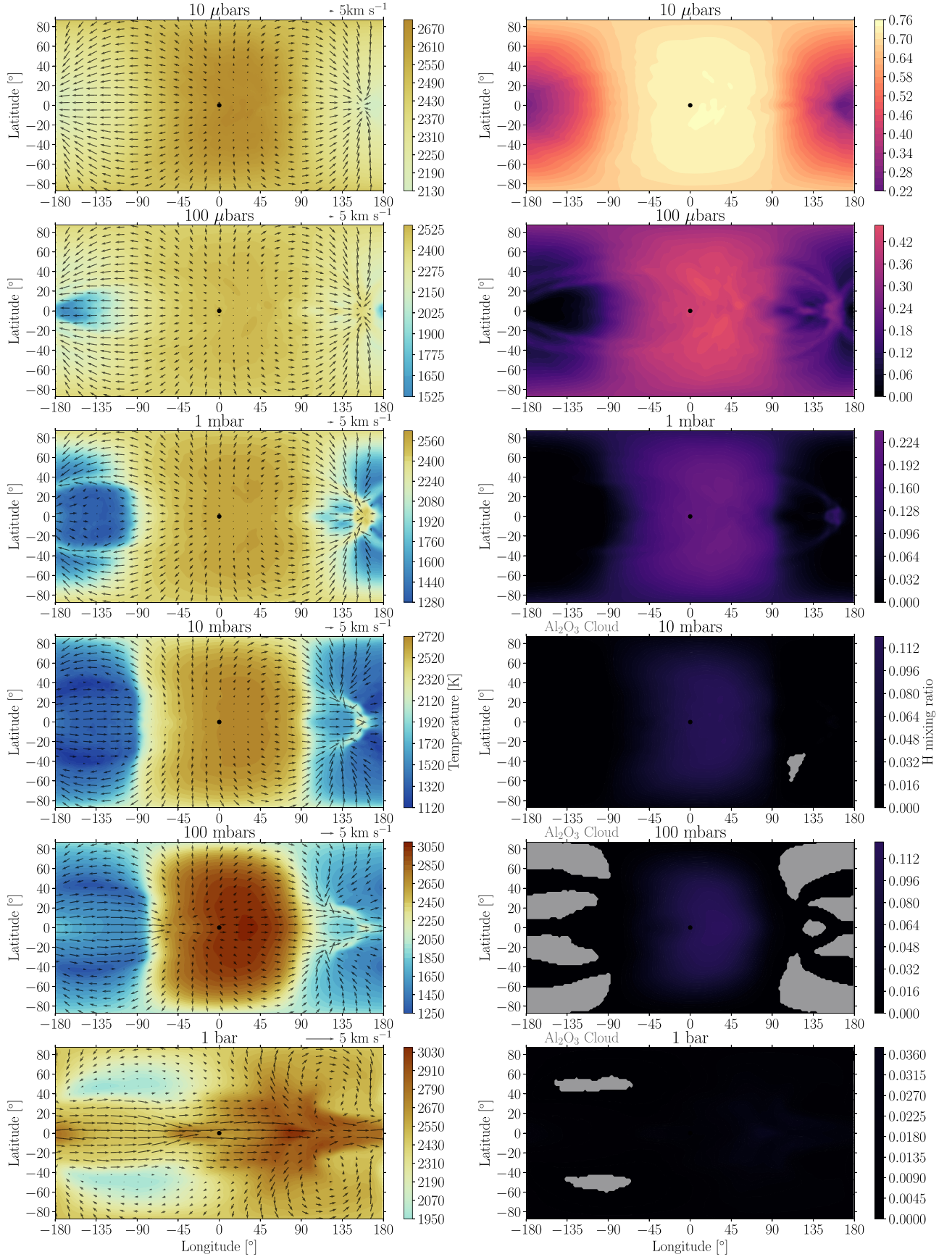


Figure 16. Temperature maps with overlaid wind arrows (left) and atomic hydrogen mass mixing ratio (right, colors) with overlaid cloud tracer distributions (gray regions show where the cloud mass mixing ratio is $\geq 5 \times 10^{-5} \text{ kg kg}^{-1}$) plotted on isobars logarithmically spaced from $10 \mu\text{bar}$ to 1 bar from the simulation with radiatively inactive clouds.

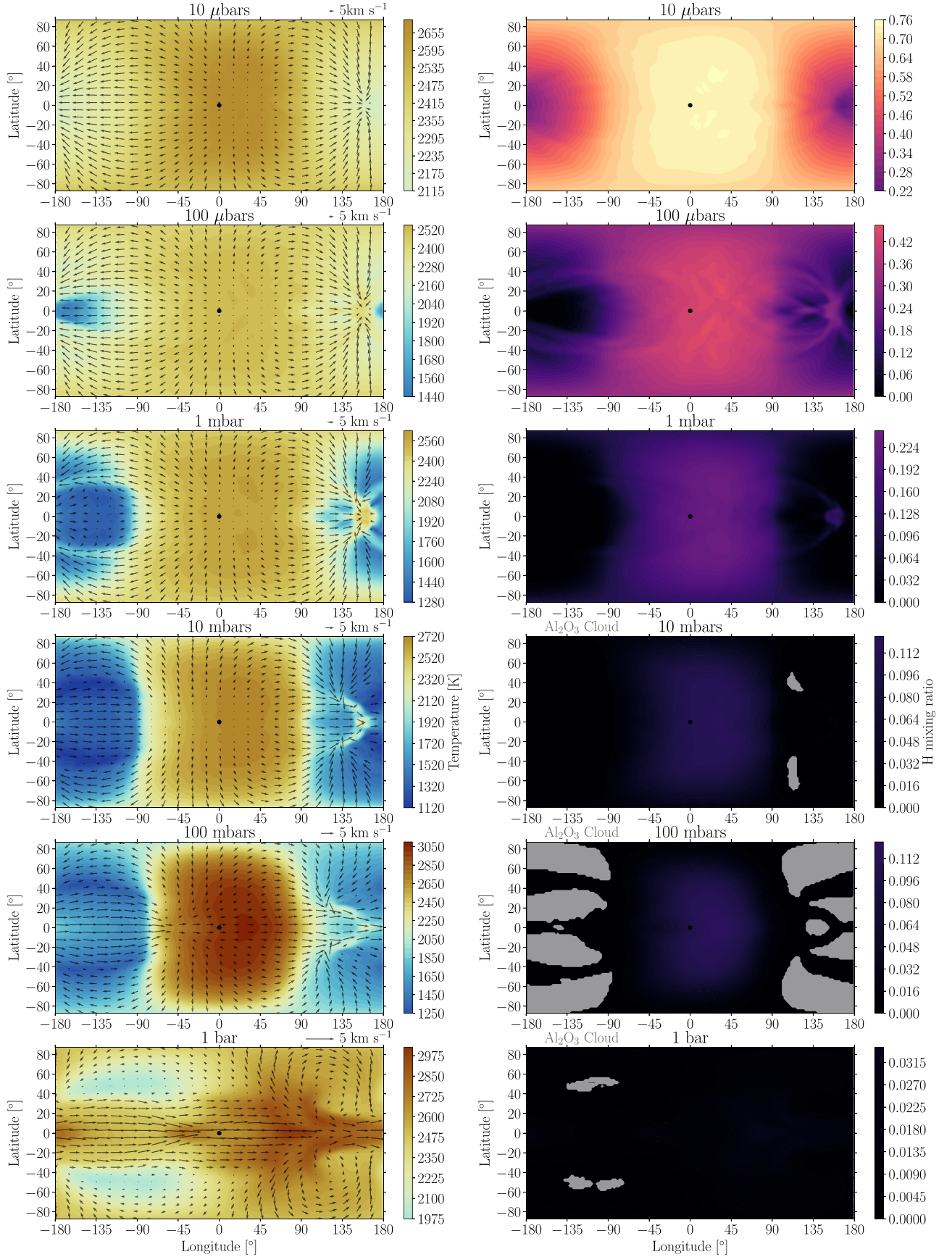


Figure 17. Temperature maps with overlaid wind arrows (left) and atomic hydrogen mass mixing ratio (right, colors) with overlaid cloud tracer distributions (gray regions show where the cloud mass mixing ratio is $\geq 5 \times 10^{-5} \text{ kg kg}^{-1}$) plotted on isobars logarithmically spaced from $10 \mu\text{bar}$ to 1 bar from the simulation with reduced cloud opacity.

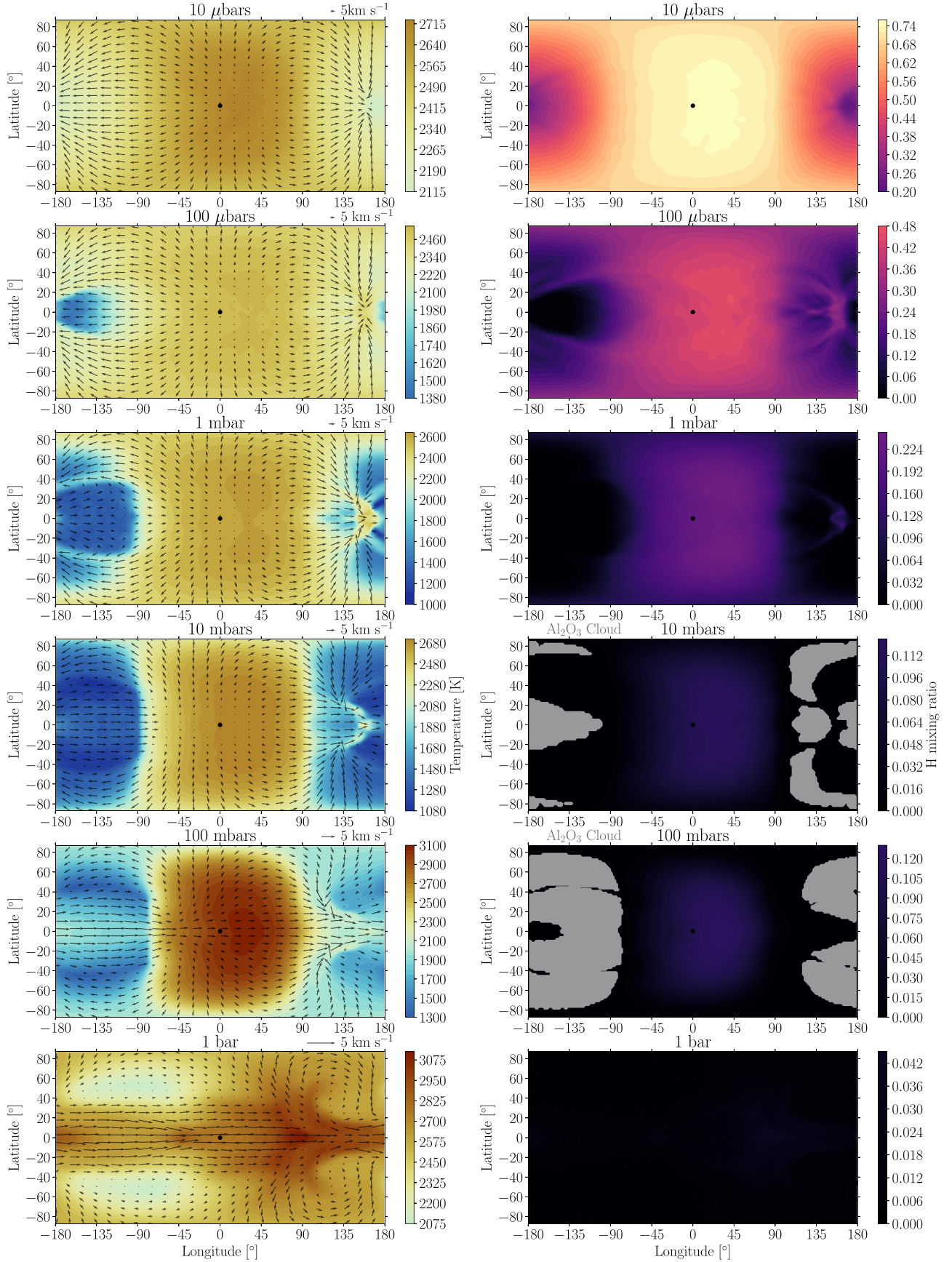


Figure 18. Temperature maps with overlaid wind arrows (left) and atomic hydrogen mass mixing ratio (right, colors) with overlaid cloud tracer distributions (gray regions show where the cloud mass mixing ratio is $\geq 5 \times 10^{-5} \text{ kg kg}^{-1}$) plotted on isobars logarithmically spaced from $10 \mu\text{bar}$ to 1 bar from the simulation with a mean cloud particle size of $r = 2 \mu\text{m}$.

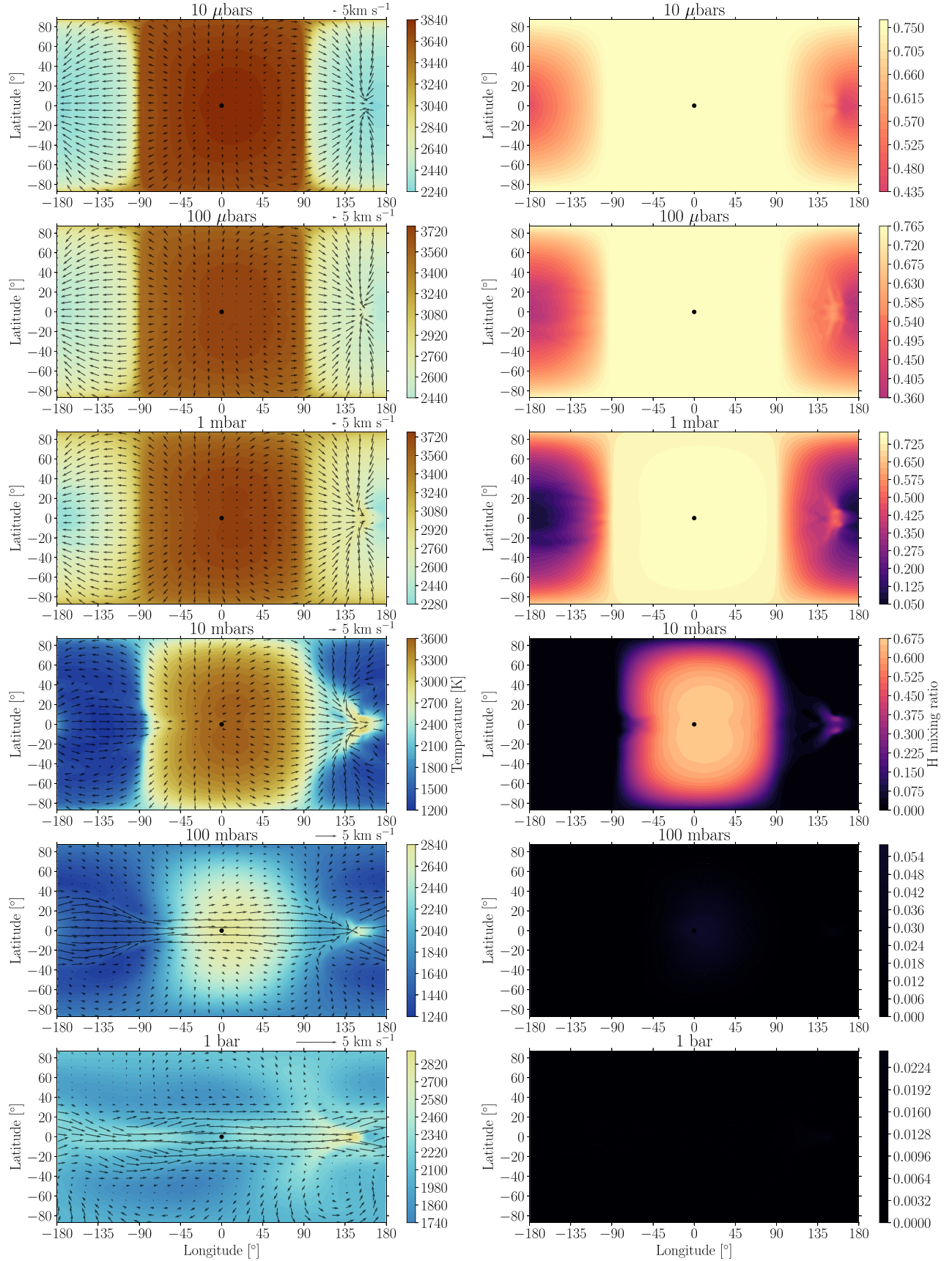


Figure 19. Temperature maps with overlaid wind arrows (left) and atomic hydrogen mass mixing ratio (right, colors) plotted on isobars logarithmically spaced from $10 \mu\text{bar}$ to 1 bar from the simulation with an enhanced visible-band opacity. Clouds with a local mass mixing ratio $\geq 5 \times 10^{-5} \text{ kg kg}^{-1}$ do not form at any location in this simulation.

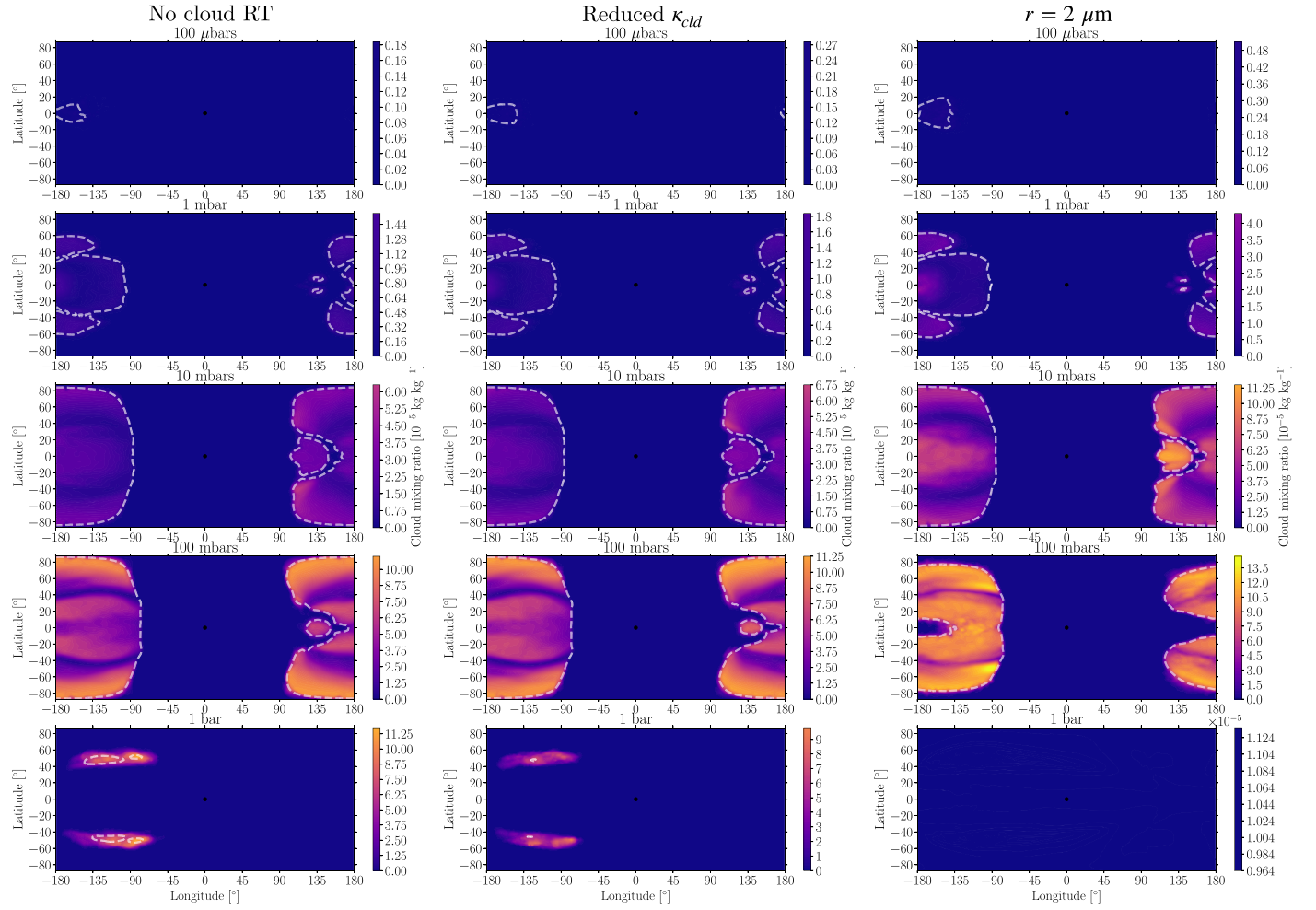


Figure 20. Maps of the cloud mass mixing ratio on isobars logarithmically spaced from 100 μ bar to 1 bar from three cases with varying cloud and radiative transfer assumptions: no cloud-radiative feedback (No cloud RT), reduced cloud opacity (Reduced κ_{cld}), and reduced mean cloud particle size ($r = 2 \mu\text{m}$). All panels share a color scale, and the cloud mixing ratio is shown in units of $10^{-5} \text{ kg kg}^{-1}$. The snow-white dashed contour displays where the gas temperature is equal to the corundum condensation temperature on each isobar.

A.2. Cloud and Condensible Vapor Mass Mixing Ratio

Figure 20 shows maps of the cloud mass mixing ratio (q_c) on isobars, while Figure 21 shows maps of the total cloud condensate and condensible vapor mass mixing ratio ($q_c + q_v$) on isobars. Both figures are equivalent to those from the baseline case shown in Figure 3 but are from the cases with varying cloud microphysical and radiative properties. The no cloud-radiative feedback and reduced cloud opacity cases have the largest differences in both cloud coverage and combined cloud plus vapor tracer distributions from the baseline case. This is due to their lack of a strong cloud-radiative feedback, which enables cloud formation at depth and shifts the cloud

deck toward higher pressures. The models without strong cloud-radiative feedback also have a significant equatorial depletion at depth in total tracer, similar to that found in previous hot Jupiter GCMs (Parmentier et al. 2013; Lines et al. 2018; Komacek et al. 2019), as shown in Figure 13 of Showman et al. (2020). The case with a reduced cloud particle size has a similar three-dimensional cloud distribution to the baseline case due to their comparable levels of cloud-radiative feedback and thus similar temperature structure and wind patterns, but with a slight increase in the maximum cloud mass mixing ratio due to the reduced settling flux of smaller cloud particles.

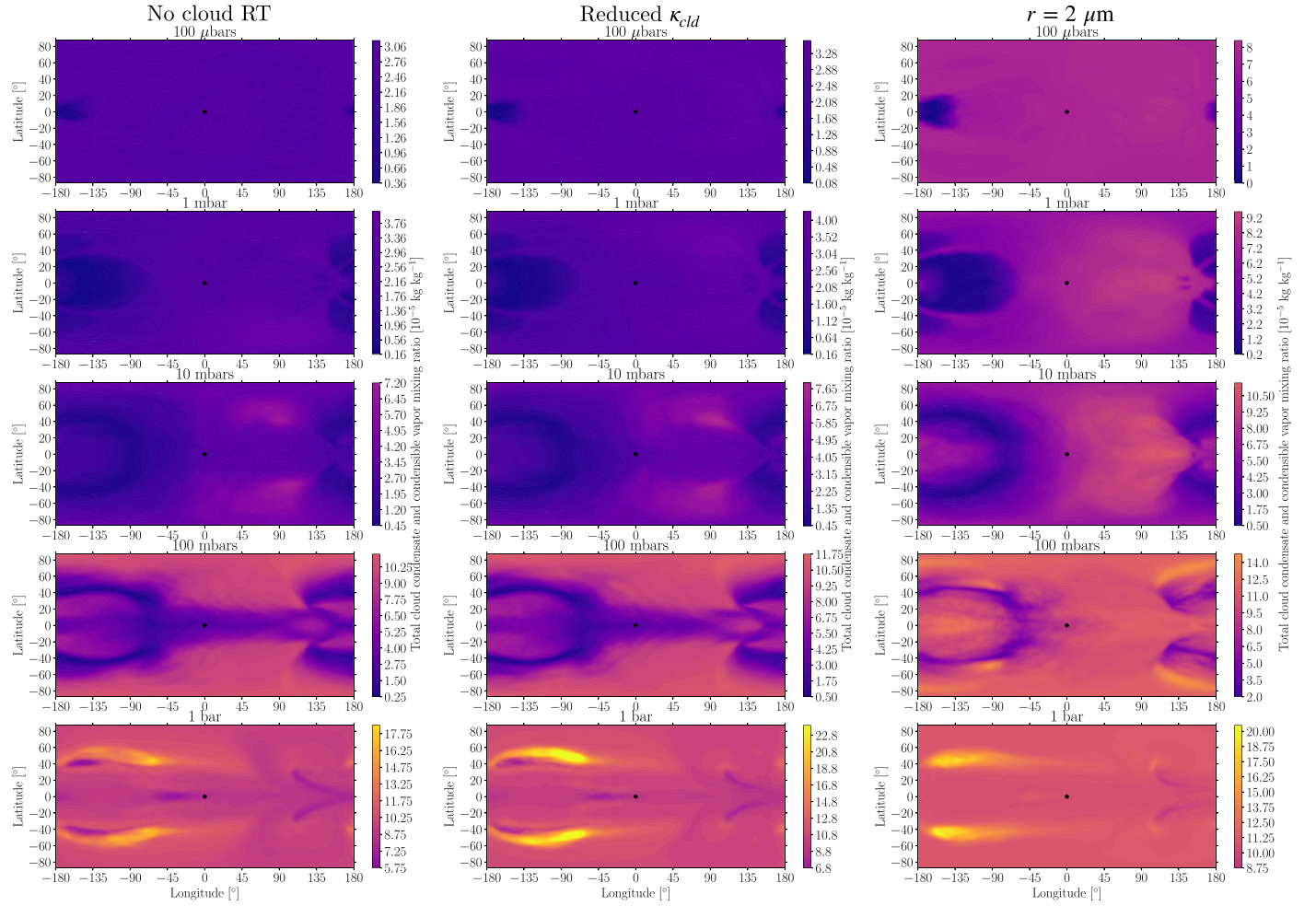


Figure 21. Maps of the total cloud condensate and condensable vapor mass mixing ratio ($q_c + q_v$) on isobars logarithmically spaced from 100 μ bar to 1 bar from three cases with varying cloud and radiative transfer assumptions: no cloud-radiative feedback (No cloud RT), reduced cloud opacity (Reduced κ_{cld}), and reduced mean cloud particle size ($r = 2 \mu\text{m}$). All panels share a color scale, and the total cloud condensate and condensable vapor mixing ratio is shown in units of $10^{-5} \text{ kg kg}^{-1}$.

A.3. Zonal-mean Zonal Wind

Figure 22 shows latitude-pressure profiles of the zonal-mean zonal wind equivalent to those from the baseline case shown in Figure 4 from the remainder of the GCM suite. The peak zonal-mean zonal wind speeds for all cases with varying cloud parameters are similarly just above 4 km s^{-1} . The no cloud-radiative transfer and reduced cloud opacity cases without a strong cloud-radiative feedback have a zonal wind maximum that is slightly more confined to high pressures than the baseline and reduced cloud particle size cases with significant cloud-radiative feedback. The largest difference in zonal-mean zonal wind structure is between the enhanced visible opacity case and all other cases, as this case has a faster peak wind speed of the equatorial jet associated with the hotter dayside and resulting larger day-to-night contrast. The eastward jet is also further confined to depth in the case with an enhanced visible opacity, showing that the transition from flow characterized by an eastward equatorial jet to predominantly day-to-night flow occurs at a higher pressure in the case with a strong thermal inversion.

A.4. Vertical Mixing

Figure 23 shows maps of the vertical pressure velocity and both cloud condensate tracer and total (cloud condensate and

condensable vapor) tracer mixing efficiency at the 100 mbar level from the cases with varying cloud parameters, equivalent to those for the baseline case shown in the bottom row of Figure 7. The pattern of vertical velocity at 100 mbar is qualitatively similar for all cases, characterized by upwelling throughout much of the dayside and local upwelling and downwelling on the nightside associated with regions of horizontal divergence and convergence, respectively. However, the spatial pattern of both the cloud and total mixing efficiencies is different between the cases with a strong cloud-radiative feedback (baseline and reduced cloud particle size) and those with a weak or nonexistent cloud-radiative feedback (reduced cloud opacity and no cloud-radiative feedback). This is due itself to the spatial differences in cloud cover, and as a result condensable vapor mixing ratio, between the cases with strong and weak cloud-radiative feedback. In the cases with stronger cloud-radiative feedback, the greater peak cloud mass mixing ratio at 100 mbar leads to larger peak absolute values of both cloud and total mixing efficiency across the 100 mbar isobar. The cases with weaker cloud-radiative feedback have a relative equatorial depletion of total tracer (see Figure 21), which in turn causes negative total mixing efficiency throughout much of the equatorial dayside. Additionally, the change in cloud pattern between cases with strong and weak cloud-radiative feedback causes

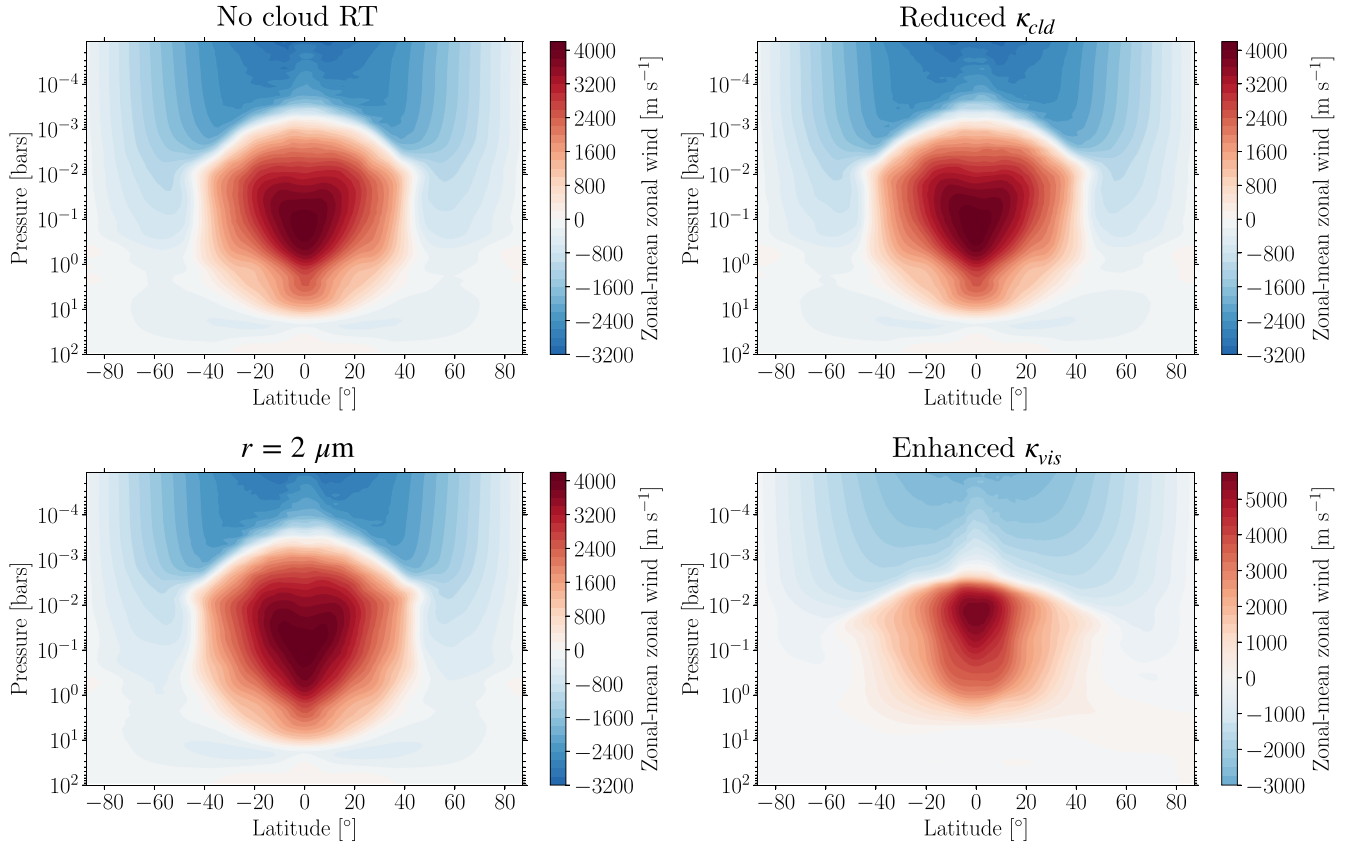


Figure 22. Zonal-mean zonal wind from four cases with varying cloud and radiative transfer assumptions: no cloud-radiative feedback (No cloud RT), reduced cloud opacity (Reduced $\kappa_{\text{cl}d}$), reduced mean cloud particle size ($r = 2 \mu\text{m}$), and enhanced visible-band opacity (Enhanced κ_{vis}).

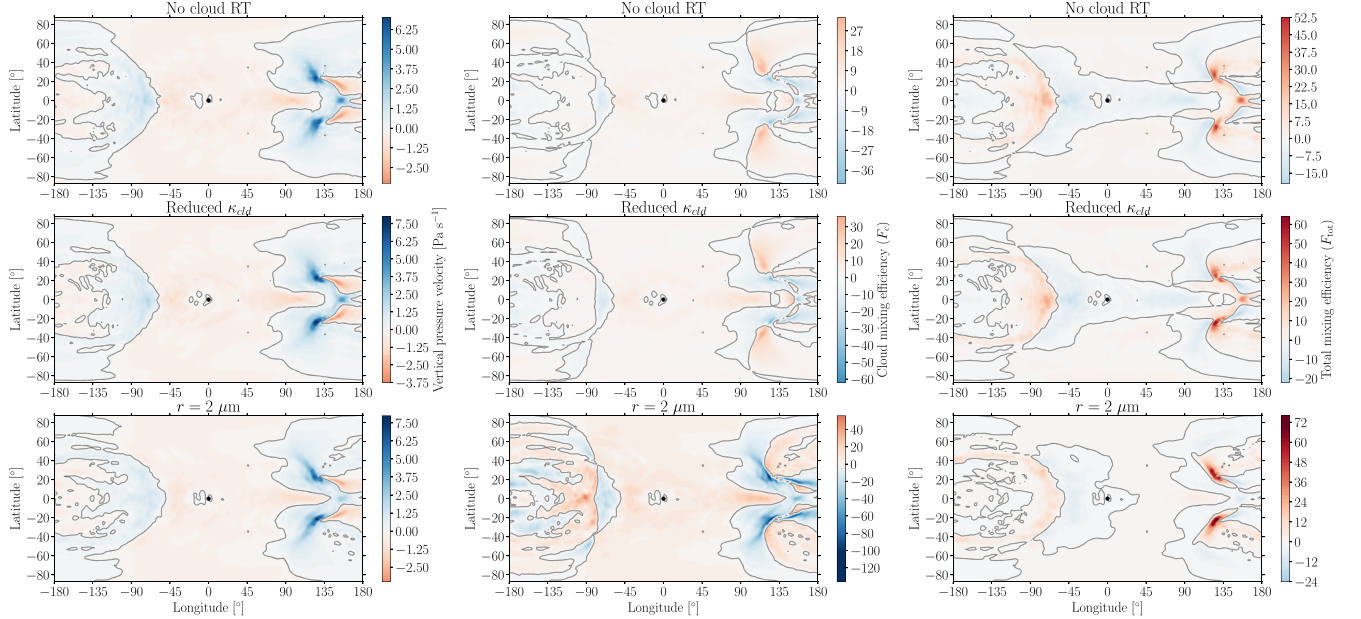


Figure 23. Vertical pressure velocity (left), cloud condensate mixing efficiency (middle), and total (cloud condensate plus condensable vapor tracer) mixing efficiency (right) at a pressure of 100 mbar for three cases with varying cloud and radiative transfer assumptions: no cloud-radiative feedback (No cloud RT), reduced cloud opacity (Reduced $\kappa_{\text{cl}d}$), and reduced mean cloud particle size ($r = 2 \mu\text{m}$). The gray contour denotes the zero velocity or mixing efficiency line. All panels for vertical velocity have separate color scales, while each column of mixing efficiency panels share a color scale. For both velocity and mixing efficiency, red corresponds to upward motion or mixing while blue corresponds to downward motion or mixing.

the regions of positive and negative cloud mixing efficiency to differ between them, as vertical motions in the same direction can either drive a positive or negative cloud mixing efficiency depending on the local value of cloud mass mixing

ratio relative to the horizontal mean on an isobar. As a result, the coupled nature of vertical winds and tracer abundance sets the amount of vertical mixing across isobars in our model suite.

ORCID iDs

Thaddeus D. Komacek  <https://orcid.org/0000-0002-9258-5311>
 Xianyu Tan  <https://orcid.org/0000-0003-2278-6932>
 Peter Gao  <https://orcid.org/0000-0002-8518-9601>
 Elspeth K. H. Lee  <https://orcid.org/0000-0002-3052-7116>

References

- Ackerman, A. S., & Marley, M. S. 2001, *ApJ*, **556**, 872
 Adams, D., Kataria, T., Batalha, N., Gao, P., & Knutson, H. 2022, *ApJ*, **926**, 157
 Adcroft, A., Hill, C., Campin, J., Marshall, J., & Heimbach, P. 2004, *MWRv*, **132**, 2845
 Addison, B., Knudstrup, E., Wong, I., et al. 2021, *AJ*, **162**, 292
 Allard, F., Homeier, D., & Freytag, B. 2012, *RSPTA*, **370**, 2765
 Allers, K., Vos, J., Biller, B., & Williams, P. 2020, *Sci*, **368**, 169
 Apai, D., Karalidi, T., Marley, M., et al. 2017, *Sci*, **357**, 683
 Arcangeli, J., Desert, J., Line, M., et al. 2018, *ApJL*, **855**, L30
 Artigau, E., Bouchard, S., Doyon, R., & Lafrenière, D. 2009, *ApJ*, **701**, 1534
 Baeyens, R., Decin, L., Carone, L., et al. 2021, *MNRAS*, **505**, 5603
 Batygin, K., Stanley, S., & Stevenson, D. 2013, *ApJ*, **776**, 53
 Batygin, K., Stevenson, D., & Bodenheimer, P. 2011, *ApJ*, **738**, 1
 Baxter, C., Désert, J., Parmentier, V., et al. 2020, *A&A*, **639**, A36
 Beatty, T., Madhusudhan, N., Tsirias, A., et al. 2017, *AJ*, **154**, 158
 Beatty, T. G., Marley, M. S., Gaudi, B. S., et al. 2019, *AJ*, **158**, 166
 Bell, T., & Cowan, N. 2018, *ApJL*, **857**, L20
 Bell, T., Dang, L., Cowan, N., et al. 2021, *MNRAS*, **504**, 3316
 Beltz, H., Rauscher, E., Brogi, M., & Kempton, E. 2021, *AJ*, **161**, 1
 Beltz, H., Rauscher, E., Roman, M., & Guillot, A. 2022, *AJ*, **163**, 35
 Berardo, D., Cumming, A., & Marleau, G. 2017, *ApJ*, **834**, 149
 Biller, B., Crossfield, I., Mancini, L., et al. 2013, *ApJL*, **778**, L10
 Bodenheimer, P., Lin, D. N. C., & Mardling, R. A. 2001, *ApJ*, **548**, 466
 Bordwell, J., Brown, B., & Oishi, J. 2018, *ApJ*, **854**, 8
 Borsa, F., Allart, R., Casasayas-Barris, N., et al. 2021, *A&A*, **645**, A24
 Cabot, H., Madhusudhan, N., Welbanks, L., et al. 2020, *MNRAS*, **494**, 363
 Caldas, A., Leconte, J., Selsis, F., et al. 2019, *A&A*, **623**, A161
 Carone, L., Baeyens, R., Mollière, P., et al. 2020, *MNRAS*, **496**, 3582
 Casewell, S., Debes, J., Braker, I., et al. 2020, *MNRAS*, **499**, 5318
 Casewell, S., Littlefair, S., Parsons, S., et al. 2018, *MNRAS*, **481**, 5216
 Chandrasekhar, S. 1939, *An Introduction to the Study of Stellar Structure* (Chicago, IL: Univ. Chicago)
 Changeat, Q. 2022, *AJ*, **163**, 106
 Cho, J., Skinner, J., & Thrastarson, H. 2021, *ApJL*, **913**, L32
 Choi, J., Dotter, A., Conroy, C., et al. 2016, *ApJ*, **823**, 102
 Christie, D., Mayne, N., Lines, S., et al. 2021, *MNRAS*, **506**, 4500
 Crossfield, I., Biller, B., Schlieder, J., et al. 2014, *Natur*, **505**, 654
 de Pater, I., Deboer, D., Marley, M., Freedman, R., & Young, R. 2005, *Icar*, **173**, 425
 Demory, B., Wit, J. D., Lewis, N., et al. 2013, *ApJL*, **776**, L25
 Dietrick, R., Mendonça, J., Schroffenegger, U., et al. 2020, *ApJS*, **248**, 30
 Dobbs-Dixon, I., & Agol, E. 2013, *MNRAS*, **435**, 3159
 Dobbs-Dixon, I., & Cowan, N. 2017, *ApJL*, **851**, L26
 Dobbs-Dixon, I., Cumming, A., & Lin, D. 2010, *ApJ*, **710**, 1395
 Dotter, A. 2016, *ApJS*, **222**, 8
 Ehrenreich, D., Lovis, C., Allart, R., et al. 2020, *Natur*, **580**, 597
 Esteves, L., de Mooij, E., & Jayawardhana, R. 2015, *ApJ*, **804**, 150
 Evans, T., Sing, D., Kataria, T., et al. 2017, *Natur*, **548**, 58
 Faherty, J., Beletsky, Y., Burgasser, A., et al. 2014, *ApJ*, **790**, 90
 Flowers, E., Brogi, M., Rauscher, E., Kempton, E., & Chiavassa, A. 2019, *AJ*, **157**, 209
 Fortney, J., Dawson, R., & Komacek, T. 2021, *JGRE*, **126**, e06629
 Fortney, J., Lodders, K., Marley, M., & Freedman, R. 2008, *ApJ*, **678**, 1419
 Freytag, B., Allard, F., Ludwig, H., Homeier, D., & Steffen, M. 2010, *A&A*, **513**, A19
 Fu, G., Deming, D., Lothringer, J., et al. 2021, *AJ*, **162**, 108
 Fu, G., Sing, D., Lothringer, J., et al. 2022, *ApJL*, **925**, L3
 Gandhi, S., & Jermyn, A. 2020, *MNRAS*, **499**, 4984
 Gandhi, S., & Madhusudhan, N. 2019, *MNRAS*, **485**, 5817
 Gandhi, S., Madhusudhan, N., & Mandell, A. 2020, *AJ*, **159**, 232
 Gao, P., & Benneke, B. 2018, *ApJ*, **863**, 165
 Gao, P., Marley, M., & Ackerman, A. 2018, *ApJ*, **855**, 86
 Gao, P., & Powell, D. 2021, *ApJL*, **918**, L7
 Gao, P., Thorngren, D., Lee, E., et al. 2020, *NatAs*, **4**, 951
 Gao, P., Wakeford, H., Moran, S., & Parmentier, V. 2021, *JGRE*, **126**, e06655
 Gelino, G., Marley, M., & Holtzman, J. 2002, *ApJ*, **577**, 433
 Gharib-Nezhad, E., Iyer, A., Line, M., et al. 2021, *ApJS*, **254**, 34
 Gierasch, P., Ingersoll, A., & Williams, R. 1973, *Icar*, **19**, 473
 Ginzburg, S., & Sari, R. 2015, *ApJ*, **803**, 111
 Glanz, H., Rozner, M., Perets, H., & Grishin, E. 2022, *ApJ*, **931**, 11
 Grimm, S., Malik, M., Kitzmann, D., et al. 2021, *ApJS*, **253**, 30
 Guillot, T. 2010, *A&A*, **520**, A27
 Guillot, T., & Guillot, A. 2002, *A&A*, **385**, 156
 Hammond, M., & Lewis, N. 2021, *PNAS*, **118**, e2022705118
 Hammond, M., & Pierrehumbert, R. 2018, *ApJ*, **869**, 65
 Harada, C., Kempton, E., Rauscher, E., et al. 2021, *ApJ*, **909**, 85
 Hartmann, D., & Larson, K. 2002, *GeoRL*, **29**, 1951
 Haynes, K., Mandell, A., Madhusudhan, N., Deming, D., & Knutson, H. 2015, *ApJ*, **806**, 146
 Helling, C., & Casewell, S. 2014, *A&ARv*, **22**, 80
 Helling, C., Lee, E., Dobbs-Dixon, I., Mayne, N., et al. 2016, *MNRAS*, **460**, 855
 Helling, C., Lewis, D., Samra, D., et al. 2021, *A&A*, **649**, A44
 Heng, K., Frierson, D., & Phillips, P. 2011, *MNRAS*, **418**, 2669
 Heng, K., & Showman, A. 2015, *Annual Reviews in Earth and Planetary Sciences*, **43**, 509
 Hindle, A., Bushby, P., & Rogers, T. 2019, *ApJL*, **872**, L27
 Hindle, A., Bushby, P., & Rogers, T. 2021a, *ApJ*, **922**, 176
 Hindle, A., Bushby, P., & Rogers, T. 2021b, *ApJL*, **916**, L8
 Hoeijmakers, H., Ehrenreich, D., Heng, K., et al. 2018, *Natur*, **560**, 453
 Hoeijmakers, H., Seidel, J., Pino, L., et al. 2020, *A&A*, **641**, A123
 Holton, J. 1986, *JGR*, **91**, 2681
 Holton, J., & Hakim, G. 2013, *An Introduction to Dynamic Meteorology* (5th edn.; New York: Academic), <https://www.elsevier.com/books/an-introduction-to-dynamic-meteorology/holton/978-0-12-384866-6>
 Hood, B., Wood, K., Seager, S., & Cameron, A. 2008, *MNRAS*, **389**, 257
 Hu, R., Demory, B., Seager, S., Lewis, N., & Showman, A. 2015, *ApJ*, **802**, 51
 Jensen, A., Cauley, P., Redfield, S., et al. 2018, *AJ*, **156**, 154
 Karalidi, T., Apai, D., Marley, M., & Buenzli, E. 2016, *ApJ*, **825**, 90
 Kasper, D., Bean, J., Line, M., et al. 2021, *ApJL*, **921**, L18
 Kataria, T., Showman, A., Lewis, N., et al. 2013, *ApJ*, **767**, 76
 Kataria, T., Sing, D. K., Lewis, N. K., et al. 2016, *ApJ*, **821**, 9
 Keating, D., Cowan, N., & Dang, L. 2019, *NatAs*, **3**, 1092
 Kempton, E., Bean, J., & Parmentier, V. 2017, *ApJL*, **845**, L20
 Kempton, E., Perna, R., & Heng, K. 2014, *ApJ*, **795**, 24
 Kempton, E., & Rauscher, E. 2012, *ApJ*, **751**, 117
 Kesseli, A., & Snellen, I. 2021, *ApJL*, **908**, L17
 Kesseli, A., Snellen, I., Casasayas-Barris, N., Mollière, P., & Sanchez-Lopez, A. 2022, *AJ*, **163**, 107
 Kippenhahn, R., Weigert, A., & Weiss, A. 2013, *Stellar Structure and Evolution* (2nd edn.; Berlin: Springer)
 Kitzmann, D., Heng, K., Rimmer, P., et al. 2018, *ApJ*, **863**, 183
 Komacek, T., & Showman, A. 2016, *ApJ*, **821**, 16
 Komacek, T., & Showman, A. 2020, *ApJ*, **888**, 2
 Komacek, T., Showman, A., & Parmentier, V. 2019, *ApJ*, **881**, 152
 Komacek, T., Showman, A., & Tan, X. 2017, *ApJ*, **835**, 198
 Komacek, T., & Tan, X. 2018, *RNAAS*, **2**, 36
 Komacek, T., Thorngren, D., Lopez, E., & Ginzburg, S. 2020, *ApJ*, **893**, 36
 Komacek, T., & Youdin, A. 2017, *ApJ*, **844**, 94
 Kreidberg, L., Line, M., Parmentier, V., et al. 2018, *AJ*, **156**, 17
 Kuang, Z., & Hartmann, D. 2007, *Jcli*, **20**, 2051
 Kylling, A., Stamnes, K., & Tsay, S. 1995, *JAIC*, **21**, 115
 Lee, E., Casewell, S., Chubb, K., et al. 2020, *MNRAS*, **496**, 4674
 Lee, E., Dobbs-Dixon, I., Helling, C., Bogner, K., & Woitke, P. 2016, *A&A*, **594**, A48
 Lee, E., Parmentier, V., Hammond, M., et al. 2021, *MNRAS*, **506**, 2695
 Lee, E., Taylor, J., Grimm, S., et al. 2019, *MNRAS*, **487**, 2082
 Lee, E., Wardenier, J., Prinoth, B., et al. 2022, *ApJ*, **929**, 180
 Lee, E., Wood, K., Dobbs-Dixon, I., Rice, A., & Helling, C. 2017, *A&A*, **601**, A22
 Lew, B., Apai, D., Zhou, Y., et al. 2016, *ApJL*, **829**, L32
 Lew, B., Apai, D., Zhou, Y., et al. 2022, *AJ*, **163**, 8
 Lewis, N., Wakeford, H., MacDonald, R., et al. 2020, *ApJL*, **902**, L19
 Line, M. R., & Parmentier, V. 2016, *ApJ*, **820**, 78
 Lines, S., Mayne, N., Manners, J., et al. 2019, *MNRAS*, **488**, 1332
 Lines, S., Mayne, N., Boutle, I., et al. 2018, *A&A*, **615**, A97
 Liu, B., & Showman, A. 2013, *ApJ*, **770**, 42
 Lodders, K. 2003, *ApJ*, **591**, 1220
 Lothringer, J., & Barman, T. 2019, *ApJ*, **876**, 69
 Lothringer, J., Barman, T., & Koskinen, T. 2018, *ApJ*, **866**, 27

- Lothringer, J., Fu, G., Sing, D., & Barman, T. 2020, *ApJL*, **898**, L14
- Lothringer, J., Sing, D., Rustamkulov, Z., et al. 2022, *Natur*, **604**, 49
- Malik, M., Kitzmann, D., Mendonça, J., et al. 2019, *AJ*, **157**, 170
- Mansfield, M., Bean, J., Line, M., et al. 2018, *AJ*, **156**, 10
- Mansfield, M., Bean, J., Stevenson, K., et al. 2020, *ApJL*, **888**, L15
- Mansfield, M., Line, M., Bean, J., et al. 2021, *NatAs*, **5**, 1224
- Marleau, G., & Cumming, A. 2014, *MNRAS*, **437**, 1378
- May, E., Komacek, T., Stevenson, K., et al. 2021, *AJ*, **162**, 158
- May, E., & Rauscher, E. 2020, *ApJ*, **893**, 161
- Mayne, N., Baraffe, I., Acreman, D., et al. 2014, *A&A*, **561**, A1
- Mayne, N., Debras, F., Baraffe, I., et al. 2017, *A&A*, **604**, A79
- Mendonça, J. 2020, *MNRAS*, **491**, 1456
- Mendonça, J., Malik, M., Demory, B., & Heng, K. 2018, *AJ*, **155**, 150
- Menou, K. 2012, *ApJ*, **745**, 138
- Menou, K. 2019, *MNRAS*, **485**, L98
- Menou, K. 2021, arXiv:2112.12127
- Menou, K., Cho, J. Y.-K., Seager, S., & Hansen, B. M. S. 2003, *ApJL*, **587**, L113
- Mikal-Evans, T., Sing, D., Barstow, J., et al. 2022, *NatAs*, **6**, 471
- Mikal-Evans, T., Sing, D., Kataria, T., et al. 2020, *MNRAS*, **496**, 1638
- Millholland, S. 2019, *ApJ*, **886**, 72
- Mol Lous, M., & Miguel, Y. 2020, *MNRAS*, **495**, 2994
- Morley, C., Marley, M., Fortney, J., & Lupu, R. 2014, *ApJL*, **789**, L14
- Morley, C. V., Fortney, J. J., Marley, M. S., et al. 2012, *ApJ*, **756**, 172
- Nugroho, S., Gibson, N., de Mooij, E., et al. 2020, *MNRAS*, **496**, 504
- Nugroho, S., Kawahara, H., Masuda, K., et al. 2017, *AJ*, **154**, 221
- Parmentier, V., & Crossfield, I. 2018, *The Exoplanet Handbook* (Berlin: Springer), 116
- Parmentier, V., Fortney, J. J., Showman, A. P., Morley, C., & Marley, M. S. 2016, *ApJ*, **828**, 22
- Parmentier, V., & Guillot, T. 2014, *A&A*, **562**, A133
- Parmentier, V., Guillot, T., Fortney, J., & Marley, M. 2015, *A&A*, **475**, A35
- Parmentier, V., Line, M., Bean, J., et al. 2018, *A&A*, **617**, A110
- Parmentier, V., Showman, A., & Fortney, J. 2021, *MNRAS*, **501**, 78
- Parmentier, V., Showman, A., & Lian, Y. 2013, *A&A*, **558**, A91
- Paxton, B., Bildsten, L., Dotter, A., et al. 2011, *ApJS*, **192**, 3
- Paxton, B., Cantiello, M., Arras, P., et al. 2013, *ApJS*, **208**, 4
- Paxton, B., Marchant, P., Schwab, J., et al. 2015, *ApJS*, **220**, 15
- Paxton, B., Schwab, J., Bauer, E., et al. 2018, *ApJS*, **234**, 34
- Paxton, B., Smolec, R., Schwab, J., et al. 2019, *ApJS*, **243**, 10
- Penn, J., & Vallis, G. 2017, *ApJ*, **842**, 101
- Penn, J., & Vallis, G. 2018, *ApJ*, **868**, 147
- Perez-Becker, D., & Showman, A. 2013, *ApJ*, **776**, 134
- Perna, R., Heng, K., & Pont, F. 2012, *ApJ*, **751**, 59
- Perna, R., Menou, K., & Rauscher, E. 2010, *ApJ*, **719**, 1421
- Pierrehumbert, R., & Hammond, M. 2019, *AnRFM*, **51**, 275
- Pino, L., Désert, J., Brogi, M., et al. 2020, *ApJL*, **894**, L27
- Pluriel, W., Zingales, T., Leconte, J., & Parmentier, V. 2020, *A&A*, **636**, A66
- Powell, D., Loudén, T., Kreidberg, L., et al. 2019, *ApJ*, **887**, 170
- Powell, D., Zhang, X., Gao, P., & Parmentier, V. 2018, *ApJ*, **860**, 18
- Prinno, B., Hoeijmakers, H., Kitzmann, D., et al. 2022, *NatAs*, **6**, 449
- Radigan, J., Jayawardhana, R., Lafrenière, D., et al. 2012, *ApJ*, **750**, 105
- Rauscher, E., & Menou, K. 2012, *ApJ*, **750**, 96
- Rauscher, E., & Menou, K. 2013, *ApJ*, **764**, 103
- Rauscher, E., Menou, K., Cho, J. Y.-K., Seager, S., & Hansen, B. M. S. 2007, *ApJL*, **662**, L115
- Robbins-Blanch, N., Kataria, T., Batalha, N., & Adams, D. 2022, *ApJ*, **930**, 93
- Rogers, T. 2017, *NatAs*, **1**, 131
- Rogers, T., & Komacek, T. 2014, *ApJ*, **794**, 132
- Rogers, T., & Mcelwaine, J. 2017, *ApJL*, **841**, L26
- Rogers, T., & Showman, A. 2014, *ApJL*, **782**, L4
- Roman, M., Kempton, E., Rauscher, E., et al. 2021, *ApJ*, **908**, 101
- Roman, M., & Rauscher, E. 2019, *ApJ*, **872**, 1
- Roth, A., Drummond, B., Hebrard, E., et al. 2021, *MNRAS*, **505**, 4515
- Sainsbury-Martinez, F., Casewell, S., Lothringer, J., Phillips, M., & Tremblin, P. 2021, *A&A*, **656**, A128
- Sainsbury-Martinez, F., Wang, P., Fromang, S., et al. 2019, *A&A*, **632**, A114
- Sarkis, P., Mordasini, C., Henning, T., Marleau, G., & Mollière, P. 2021, *A&A*, **645**, A79
- Savel, A., Kempton, E., Malik, M., et al. 2022, *ApJ*, **926**, 85
- Schneider, A., Carone, L., Decin, L., et al. 2022, arXiv:2202.09183
- Schwartz, J., & Cowan, N. 2015, *MNRAS*, **449**, 4192
- Seeley, J., Jeevanjee, N., & Romps, D. 2019, *GeoRL*, **46**, 1842
- Seidel, J., Ehrenreich, D., Allart, R., et al. 2021, *A&A*, **653**, A73
- Seidel, J., Ehrenreich, D., Pino, L., et al. 2020, *A&A*, **633**, A86
- Seidel, J., Ehrenreich, D., Wyttenbach, A., et al. 2019, *A&A*, **623**, A166
- Seiff, A., Kirk, D. B., Knight, T. C. D., et al. 1998, *JGR*, **103**, 22857
- Sheppard, K., Mandell, A., Tamburo, P., et al. 2017, *ApJL*, **850**, L32
- Showman, A., & Dowling, T. 2000, *Sci*, **289**, 1737
- Showman, A., Fortney, J., Lewis, M., & Shabram, M. 2013, *ApJ*, **762**, 24
- Showman, A., Fortney, J., Lian, Y., et al. 2009, *ApJ*, **699**, 564
- Showman, A., & Guillot, T. 2002, *A&A*, **385**, 166
- Showman, A., & Kaspi, Y. 2013, *ApJ*, **776**, 85
- Showman, A., & Polvani, L. 2011, *ApJ*, **738**, 71
- Showman, A., Tan, X., & Parmentier, V. 2020, *SSRv*, **216**, 139
- Showman, A., Tan, X., & Zhang, X. 2019, *ApJ*, **883**, 4
- Sing, D., Lavvas, P., Ballester, G., et al. 2019, *AJ*, **158**, 91
- Sing, D., Fortney, J. J., Nikolov, N., et al. 2016, *Natur*, **529**, 59
- Stamnes, K., Tsay, S., Wiscombe, W., & Jayaweera, K. 1988, *ApOpt*, **27**, 2502
- Stangret, M., Palle, E., Casasayas-Barris, N., et al. 2021, *A&A*, **654**, A73
- Steinrueck, M., Showman, A., Lavvas, P., et al. 2021, *MNRAS*, **504**, 2783
- Stevenson, K., Bean, J., Madhusudhan, N., & Harrington, J. 2014, *ApJ*, **791**, 36
- STScI Development Team 2013, pypsnphot: Synthetic photometry software package, Astrophysics Source Code Library, ascl:1303.023
- Taberner, H., Osorio, M. Z., Allart, R., et al. 2021, *A&A*, **646**, A158
- Tan, X. 2022, *MNRAS*, **511**, 4861
- Tan, X., & Komacek, T. 2019, *ApJ*, **886**, 26
- Tan, X., & Showman, A. 2017, *ApJ*, **835**, 186
- Tan, X., & Showman, A. 2019, *ApJ*, **874**, 111
- Tan, X., & Showman, A. 2020, *ApJ*, **902**, 27
- Tan, X., & Showman, A. 2021a, *MNRAS*, **502**, 678
- Tan, X., & Showman, A. 2021b, *MNRAS*, **502**, 2198
- Thorngren, D., & Fortney, J. 2018, *AJ*, **155**, 214
- Thorngren, D., Gao, P., & Fortney, J. 2019, *ApJL*, **884**, L6
- Thorngren, D. P., Fortney, J. J., Murray-Clay, R. A., & Lopez, E. D. 2016, *ApJ*, **831**, 64
- Tremblin, P., Bloch, H., González, M., et al. 2021, *A&A*, **653**, A30
- Tremblin, P., Chabrier, G., Mayne, N., et al. 2017, *ApJ*, **841**, 30
- Tsai, S., Dobbs-Dixon, I., & Gu, P. 2014, *ApJ*, **793**, 141
- Vallis, G. K. 2017, *Atmospheric and Oceanic Fluid Dynamics* (Cambridge: Cambridge Univ. Press), doi:10.1017/9781107588417
- Visscher, C., Loders, K., & Fegley, B., Jr 2010, *ApJ*, **716**, 1060
- Vos, J., Faherty, J., Gagné, J., et al. 2022, *ApJ*, **924**, 68
- Wakeford, H., Sing, D., Stevenson, K., et al. 2020, *AJ*, **159**, 204
- Wakeford, H. R., Visscher, C., Lewis, N. K., et al. 2017, *MNRAS*, **464**, 4247
- Wang, H., & Wordsworth, R. 2020, *ApJ*, **891**, 7
- Wardenier, J., Parmentier, V., & Lee, E. 2022, *MNRAS*, **510**, 620
- Wardenier, J., Parmentier, V., Lee, E., Line, M., & Gharib-Nezhad, E. 2021, *MNRAS*, **506**, 1258
- Wilson, J., Gibson, N., Nikolov, N., et al. 2020, *MNRAS*, **497**, 5155
- Wing, A., Stauffer, C., Becker, T., et al. 2020, *JAMES*, **12**, e02138
- Wong, I., Shporer, A., Zhou, G., et al. 2021, *AJ*, **162**, 256
- Wong, I., Shporer, A., Morris, B., et al. 2020, *AJ*, **160**, 88
- Wu, Y., & Lithwick, Y. 2013, *ApJ*, **763**, 13
- Yan, F., Pallé, E., Reiniers, A., et al. 2020, *A&A*, **640**, L5
- Yan, F., Reiniers, A., Pallé, E., et al. 2022, *A&A*, **659**, A7
- Young, R., Read, P., & Wang, Y. 2019, *Icar*, **326**, 225
- Zelinka, M., & Hartmann, D. 2010, *JGRD*, **115**, D16117
- Zhang, J., Kempton, E., & Rauscher, E. 2017, *ApJ*, **851**, 84
- Zhang, X. 2020, *RAA*, **20**, 099
- Zhang, X., & Showman, A. 2017, *ApJ*, **836**, 73
- Zhang, X., & Showman, A. 2018a, *ApJ*, **886**, 1
- Zhang, X., & Showman, A. 2018b, *ApJ*, **866**, 2
- Zhou, Y., Apai, D., Tan, X., et al. 2022, *AJ*, **163**, 17